

Anisotropic gap structure and sign reversal symmetry in monolayer Fe(Se,Te)

Yu Li^a, Dingyu Shen^a, Andreas Kreisel^b, Cheng Chen^a, Tianheng Wei^a, Xiaotong Xu^a & Jian Wang^{a,c,d,e,1}

^aInternational Center for Quantum Materials, School of Physics, Peking University, Beijing 100871, China.

^bInstitut für Theoretische Physik, Universität Leipzig, D-04103 Leipzig, Germany.

^cCollaborative Innovation Center of Quantum Matter, Beijing 100871, China.

^dCAS Center for Excellence in Topological Quantum Computation, University of Chinese Academy of Sciences, Beijing 100190, China.

^eBeijing Academy of Quantum Information Sciences, Beijing 100193, China.

¹To whom correspondence may be addressed. Email: jianwangphysics@pku.edu.cn.

Author Contributions: J.W. conceived and instructed the research. Y.L. and C.C. prepared the samples and carried out the STM/STS experiments. Y.L., D.S., X.X., and T.W. analyzed the experimental data. D.S. and A.K. performed the theoretical analysis and calculations. Y.L., D.S., and J.W. wrote the manuscript with comments from all authors.

Competing Interest Statement: The authors declare that they have no competing interests.

Classification: Physical Sciences, Physics

Keywords: high-temperature superconductors | anisotropic superconducting gap | s_{\pm} -wave pairing symmetry | quasiparticle interference | scanning tunneling spectroscopy

Abstract

The iron-based superconductors are an ideal platform to reveal the enigma of the unconventional superconductivity and potential topological superconductivity. Among them, the monolayer Fe(Se,Te)/SrTiO₃(001), which is proposed to be topological nontrivial, shows interface-enhanced high-temperature superconductivity in the two dimensional limit. However, the experimental studies on the superconducting pairing mechanism of monolayer Fe(Se,Te) films are still limited. Here, by measuring quasiparticle interference in monolayer Fe(Se,Te)/SrTiO₃(001), we report the observation of the anisotropic structure of the large superconducting gap and the sign change of the superconducting gap on different electron pockets. The results are well consistent with the ‘bonding-antibonding’ s_{\pm} -wave pairing symmetry driven by spin fluctuations in conjunction with spin-orbit coupling. Our work is of basic significance not only for a unified superconducting formalism in the iron-based superconductors, but also for understanding of topological superconductivity in high-temperature superconductors.

Significance Statement

The pairing mechanism has always been one of the most challenging problems in high-temperature superconductors. While the electron-hole Fermi pocket nesting scenario has been widely accepted for iron-based superconductors, the pairing mechanism is still under debate in the monolayer FeSe-based system, due to the absence of hole pockets. Here, by analyzing quasiparticle interference in monolayer Fe(Se,Te)/SrTiO₃(001), a high-temperature topological superconductor candidate, we uncover an

anisotropic superconducting gap structure and a sign reversal symmetry. These results are consistent with the ‘bonding-antibonding’ s_{\pm} -wave pairing symmetry, which can be driven by spin fluctuations in conjunction with spin-orbit coupling. Our work indicates a unified understanding of pairing mechanism in iron-based superconductors and provides a valuable knowledge for the study of high-temperature topological superconductivity.

Introduction

Among iron-based superconductors (FeBSs), the monolayer FeSe film grown on SrTiO₃(001) substrate (1-UC FeSe/STO) with an impressively large superconducting (SC) gap of almost 20 meV via scanning tunneling microscopy/spectroscopy (STM/STS) (1) and onset SC transition temperature (T_c) of above 40 K via electrical-transport measurement (2), has fueled intensive experimental and theoretical researches upon its SC properties and pairing mechanism (3-8). Despite numerous researches, both the SC gap structure and gap symmetry, which are prerequisites to understand the microscopic pairing mechanism, are still under debate (9-11). Specifically, early studies showed that the SC gaps of the electron pockets at the corner (\tilde{M}) of the Brillouin zone (BZ) were nearly isotropic (6, 7). However, later high-resolution angle-resolved photoemission spectroscopy studies claimed that the SC gaps were moderately anisotropic on the electron pockets (8). As for the gap symmetry, due to electron doping, the hole pocket in the center (Γ) of the BZ sinks entirely below the Fermi energy in 1-UC FeSe/STO (12), which challenges the widely accepted s_{\pm} -wave pairing within the electron-hole Fermi pocket nesting picture in FeBSs (13). Alternative pairing symmetries were theoretically proposed, including s_{++} -wave (14, 15), ‘bonding-antibonding’ s_{\pm} -wave (16, 17), and ‘quasi-nodeless’ d -wave (18, 19). Unfortunately, a consensus of the pairing symmetry is still lacking, owing to the experimental difficulty to completely distinguish ‘bonding-antibonding’ s_{\pm} -wave from ‘quasi-nodeless’ d -wave and the incompatible experimental evidences supporting s_{++} -wave (20) and ‘bonding-antibonding’ s_{\pm} -wave (21), respectively. Recently, 1-UC Fe(Se,Te)/STO has been predicted to be topological nontrivial with T_c comparable to that of the 1-UC FeSe/STO and much higher than bulk Fe(Se,Te) (22-25). Robust zero-energy bound states at both ends of atomic line defects in 1-UC Fe(Se,Te)/STO, as a signature of Majorana bound states, have been detected (26, 27). However, the experimental results related to either gap structures or a direct visualization of gap signs in 1-UC Fe(Se,Te)/STO are entirely absent. Thus, the researches on the pairing mechanism in 1-UC Fe(Se,Te)/STO are highly desired for understanding both high T_c and topological superconductivity.

Quasiparticle interference (QPI) measurement has been established as a powerful tool to characterize electronic states in superconductors (28-34), where the Bogoliubov quasiparticles located at the SC gap edge or at the in-gap bound states naturally inherit the amplitude and phase information of SC order parameters. Specifically, QPI is designed for measuring the modulation of the differential conductance mappings $g(\mathbf{r}, E) = dI/dV(\mathbf{r}, eV)$, resulting from interference of quasiparticles scattered by defects. After the Fourier transform (FT), the resultant FT-QPI signal is a complex function expressed as $g(\mathbf{q}, E) = |g(\mathbf{q}, E)|\exp(i\theta_{\mathbf{q}, E})$, where \mathbf{q} is the momentum transfer of the scattering momenta \mathbf{k} on the Fermi pockets ($\mathbf{q} = \mathbf{k}_1 - \mathbf{k}_2$). The intensity of the FT-QPI patterns $|g(\mathbf{q}, E)|$ can provide valuable information about the precise shape of the Fermi surfaces (FSs) and the momentum space (\mathbf{k} -space) structure of SC gaps (30, 31). Moreover, the scattering phase $\theta_{\mathbf{q}, E}$ encodes crucial messages about the sign of SC gaps, which can be analyzed by phase-referenced QPI (PR-QPI) methods. The sign of SC gaps is critical to explicitly distinguish the gap symmetry and further deduce the pairing interaction (32-34). Therefore, QPI measurement is a quantitative method

to study the amplitude and phase of SC order parameters and can reveal the SC pairing mechanism.

In this work, we measured and analyzed the FT-QPI patterns in 1-UC Fe(Se,Te)/STO to investigate the SC pairing mechanism. By fitting the tunneling spectra and utilizing the FT-QPI patterns to quantitatively extract the gap structure, we detected a highly anisotropic SC gap on the outer electron pocket at \tilde{M} . We further proposed a PR-QPI method and used it to verify the sign change between the SC gaps on the outer and inner electron pockets. The determination of the anisotropic gap and visualization of the sign reversal gaps are well consistent with ‘bonding-antibonding’ s_{\pm} -wave scenario (16, 17). Our work provides a valuable knowledge for a high T_c topological superconductor candidate and contributes to a unified understanding of pairing mechanism in FeBSs.

Results

Superconducting gap fitting with Dynes model. The 1-UC Fe(Se,Te) film was epitaxially grown on a SrTiO₃(001) substrate by molecular beam epitaxy (26) (see Methods for details). The nominal ratio of Se/Te (0.5/0.5) was estimated from the thickness of the second-layer Fe(Se,Te) film (25, 26) (Supplementary Text 1.1 and Fig. S1). The STM topographic atomic-resolution image shows the topmost Se/Te atom arrangement of the 1-UC Fe(Se,Te) film (Fig. 1A). The square lattice of top layer Se/Te atom corresponds to the two-iron (2-Fe) unit cell, which is depicted as the dashed black box in the crystal structure as shown in Fig. 1B. The typical tunneling spectrum exhibits two pairs of pronounced coherence peaks and remarkable U-shaped SC gaps at 4.3 K (Fig. 1C, top panel), indicating a fully gapped quasiparticle excitation spectrum and nodeless pairing symmetry. By locating the zero points of the second derivative of conductance d^2I/dV^2 (Fig. 1C, bottom panel), we could directly determine the two SC gaps of $|\Delta_1| = 11 \pm 0.1$ meV and $|\Delta_2| = 18.5 \pm 0.3$ meV, comparable to our early results (26). Originating from the band edge effect (35), the tunneling spectrum is quite asymmetric with density of states much higher at positive bias voltage than the negative bias side, which holds even after the normalization (Fig. 1C, middle panel). In addition, the tunneling spectrum displays an obvious hump feature outside the SC gaps (Fig. 1C, orange area), which implies the bosonic mode and is consistent with our previous results (36). We further symmetrized the spectrum by averaging the negative bias side and the positive bias side of the normalized spectrum and picked the bosonic-coupling-unmodified bias region $[-25, 25]$ mV for the Dynes model fitting (Fig. 1D). Strikingly, the two-band anisotropic Dynes formula expresses reasonable fittings (Fig. 1D) with anisotropic pairing strength of $|\Delta_1^{max}| = 9.55 \pm 0.15$ meV and $|\Delta_2^{max}| = 18.13 \pm 0.08$ meV (Fig. 1E). The obtained gap values show moderate decrease compared to those determined by d^2I/dV^2 , since the Dynes model takes into account the thermal broadening stemming from finite-lifetime effects of the quasiparticles at the gap edge (37, 38). As for two-band Dynes model fitting without incorporating SC gap anisotropy, while the tunneling spectrum can be fitted, the obtained parameters of $|\Delta_{1,2}|$ are physically irrational (Supplementary Text 1.2 and Fig. S2). Besides, after including gap anisotropy, even one-band Dynes model fitting can give superficially satisfying results (Supplementary Text 1.2 and Fig. S2). However, from a theoretical perspective, the band folding and hybridization in BZ of 2-Fe unit cell shall naturally recombine the two elliptic-shaped electron pockets into the inner and outer pockets (Fig. 2B). Then the newly formed inner and outer pockets will possess distinct gap functions (14, 19). Therefore, by comparing different types of Dynes model fittings, a noticeable anisotropy of SC gaps is revealed in 1-UC Fe(Se,Te)/STO. Furthermore, we averaged over 180 spectra to represent a general tunneling spectrum and repeated the above-mentioned data processing procedure and Dynes model fittings. This control experiment yields the same anisotropic SC gaps (Figs. S1 and S3), which

validates the universality of the gap anisotropy, whereas the direction of the gap maxima in the BZ and the gap sign cannot be obtained by Dynes model fittings.

Identification of scattering wave vectors in FT-QPI pattern. The Bogoliubov quasiparticles, elastically scattered by defects (see Supplementary Text 1.3 and Fig. S4 for defect information), form the standing wave patterns which can be visualized by differential conductance mappings $g(\mathbf{r}, E)$ in real space (\mathbf{r} -space) at energy E (Fig. 2A). Before the FT, the $g(\mathbf{r}, E)$ was corrected by the Lawler-Fujita algorithm (39) to reduce the distortions of the non-orthogonality in the x/y axes (Supplementary Note 2.1 and Fig. S5). The FT-QPI pattern was further symmetrized in order to increase the signal-to-noise ratio. Then we suppressed the intensity of very small scattering vectors around the center, since they stem from long range spatial variations of the surface and from randomly distributed defects, which occasionally obscure the visibility of the central scattering contour (Supplementary Note 2.2 and Fig. S6). The obtained FT-QPI pattern $|g(\mathbf{q}, E)|$ clearly shows three types of ring-like scattering structures (Fig. 2C and Fig. S7 for full FT-QPI data), which can be understood by the FSs geometry in the folded BZ (Fig. 2B). Here, \mathbf{q}_1 denotes the scattering vector within electron pockets at the same \tilde{M} point, and we use \mathbf{q}_1 ring to represent the central scattering pattern. \mathbf{q}_2 and \mathbf{q}_3 are contributed by scatterings between the nearest-neighboring and next nearest-neighboring electron pockets, and we use \mathbf{q}_2 and \mathbf{q}_3 rings to denote corresponding scattering patterns (Fig. 2C). It is widely accepted that the staggered arrangement of Se/Te atoms doubles the primitive unit cell, folding the electron pockets on top of each other. However, an underappreciated fact is that the pockets do not become identical replicas and the folded bands appear to have weaker spectral weight in the folded BZ (20, 40) (gray dashed ellipses in Fig. 2B). As a result, the \mathbf{q}_1 , \mathbf{q}_2 and \mathbf{q}_3 scattering patterns do not have identical geometries, though they only differ by reciprocal vectors in the folded BZ (Fig. 2C). We discussed that the different scattering patterns are related to different Fe 3d orbitals in Supplementary text 3 and Fig. S8. In the following, we mainly concentrate on \mathbf{q}_1 ring, because it is best visualized in experiments and contains the most comprehensive information.

Figure 2D clearly shows the \mathbf{q}_1 ring with two schematically plotted ellipses to roughly outline the contour. Actually, because of the band hybridization deriving from spin-orbit coupling (SOC) (14, 17, 19), the two elliptic-shaped electron pockets shall be recombined into inner and outer pockets marked as δ_1 and δ_2 in Fig. 2B respectively. Accordingly, \mathbf{q}_1 ring should have three sub-sets, comprising intra-pocket scatterings of inner and outer pockets ($\delta_1 \leftrightarrow \delta_1$, $\delta_2 \leftrightarrow \delta_2$) as well as inter-pocket scatterings between them ($\delta_1 \leftrightarrow \delta_2$). However, the three sub-sets of \mathbf{q}_1 ring are not distinctively resolved in our FT-QPI patterns. Instead, the ring seems to have noticeable width (Fig. 2D), especially in the $\Gamma\tilde{M}$ directions ($\theta = 45^\circ + 90^\circ \times N$, $N = 0, 1, 2, 3$). This may arise from the intrinsically close distance between inner and outer pockets, as well as our limited \mathbf{q} -resolution of the FT-QPI pattern. Consequently, the three scattering channels mix together in our FT-QPI patterns and are observed as the broadening of the ring. Notwithstanding, by extracting the line cuts of FT-QPI intensity $|g(\mathbf{q}, E)|$ along different radial direction and locating the maximum of each line cut, we can more precisely track the contour of \mathbf{q}_1 scattering pattern (Supplementary Text 4.1 and Fig. S9).

Determination of the gap structure from central FT-QPI pattern. When SC gap ($\Delta(\mathbf{k})$) is anisotropic in \mathbf{k} -space, the constant-energy contours (CECs) of Bogoliubov quasiparticle at a given energy (E) within gap minimum and gap maximum, are roughly banana-shaped (Fig. 3A, red contours), and the tips of the CECs, i.e. ‘banana’ tips (Fig. 3A, red solid dots) possess a gap value equal to the

energy of CECs ($\Delta(\mathbf{k}) = E$) (30, 31). More importantly, since the locus of the ‘banana’ tips have the highest spectral weight, the scattering vectors connecting the tips should have maximum intensity in FT-QPI pattern (30, 31). Then, by tracking the evolution of the maximum-intensity points associated with these ‘banana’ tips, one can quantitatively extract the \mathbf{k} -space structure of the anisotropic gap and simultaneously obtain the shape of the FS (30, 31).

To extract the structure of the large SC gap ($|\Delta_2(\mathbf{k})|$), we adopted an approach, previously applied on LiFeAs (30). This approach is based on the maximum-intensity points along a specific high-symmetry direction, i.e. the gap minimum direction. The scattering vectors associated with ‘banana’ tips (Fig. 3, A and B, arrows) are strictly along this direction, which is guaranteed by the C_4 symmetry of the electronic structure (see Supplementary Text 2.2 for clarification of C_4 symmetry). At a given energy E within anisotropic gap value (Fig. 3, A and B, arrows with same color), the scattering vectors naturally have two different lengths, with the shorter one (Fig. 3, A and B, $\mathbf{q}_M^{t_1}$) associated with the ‘banana’ tips within one CEC, and the longer one (Fig. 3, A and B, $\mathbf{q}_M^{t_2}$) associated with the ‘banana’ tips between two CECs. When the E changes from gap minimum ($|\Delta_2^{min}|$) to gap maximum ($|\Delta_2^{max}|$), these maximum-intensity points would form a curve, shown as the red dashed curve in Fig. 3B. This curve not only reflects the anisotropic structure of the SC gap, but also can be used to obtain the FS (see Supplementary Text 4.2 and Fig. S10 for the method to obtain FS). Besides, the orange dashed curve in Fig. 3B represents the band dispersion $E(\mathbf{q}) = E(2\mathbf{k})$. It derives from the opposite-side scatterings ($\mathbf{k} \leftrightarrow -\mathbf{k}$) between the CECs at the gap minimum direction, rather than associated with the ‘banana’ tips.

Since the SC coherence peak in the tunneling spectrum is theoretically located at the gap maximum (30, 31), we can recognize that the gap maximum is about 18 meV from the average tunneling spectrum (Fig. S1c). When energy below the gap maximum, FT-QPI intensity is supposed to be suppressed along the gap maximum direction (30, 41), and the location where FT-QPI intensity first emerges would naturally relates to the gap minimum direction. By extracting the intensity of \mathbf{q}_1 scattering pattern (Supplementary Text 4.1 and Fig. S9), we observed that the intensity is relatively faint in the $\Gamma\tilde{X}$ directions ($\theta = 0^\circ + 90^\circ \times N$) compared to that of $\Gamma\tilde{M}$ directions (Fig. S11c). Therefore, we extracted the line cuts of FT-QPI intensity along the radial direction at $\theta = 45^\circ$ ($\Gamma\tilde{M}$), i.e. the gap minimum direction. The intensity is plotted in a $|\mathbf{q}|-E$ plane (Fig. 3C). By locating the maximum-intensity points in the $|\mathbf{q}|-E$ plane (Fig. 3C, hollow dots), we obtained the two curved trajectories (Fig. 3C, red and orange dashed curves) as expected. Besides, one may argue that the maximum-intensity points also appear at E from 10 meV to 12 meV and within $|\mathbf{q}|$ from $0.2 \pi/a_0$ to $0.3 \pi/a_0$ (Fig. 3C, bottom-left). These points form a ‘ Λ ’ line shape, which mimics the curved trajectory at higher energy, and possibly originate from the scattering between inner CECs ($\delta_1 \leftrightarrow \delta_1$).

The orange dashed curve in Fig. 3C shows the electron-like branch of Bogoliubov spectrum ($E_k = \pm\sqrt{\Delta_k^2 + \varepsilon_k^2}$), which deviates from the normal band dispersion (20), when approaching the edge of the SC gap ($E_k \rightarrow \Delta_k$). The red dashed curve in Fig. 3C connects maximum-intensity points associated with ‘banana’ tips. The energy evolution contains the information about the gap structure. Firstly, the peak of the trajectory reveals that the gap maximum is around 18 meV, which is consistent with the energy of the coherence peak in the averaged tunneling spectrum. Secondly, the gap minimum determined by the intersection point of the two trajectories is around 10 meV, which can be verified by the PR-QPI patterns as shown in the following section. Thirdly, we show the measured \mathbf{k} -space structure of the anisotropic SC gap on the simultaneously obtained FS in Fig. 3D. The FS is square-shape, in accordance with the theoretical geometry of the outer pocket δ_2 formed by SOC induced

band hybridization (14, 17, 19). As discussed in Supplementary Text 4.3, another approximate approach (42) is adopted to double check the gap structure. A comparison of Fig. S11 with Fig. 3D reveals that both methods yield the same result.

Sign-reversal SC gaps revealed by PR-QPI. In addition to the gap structure, another key characteristic of SC order parameters is the gap symmetry, which intimately relates to the scattering phase in QPI measurement. However, early PR-QPI methods developed for cuprates encounter difficulties when applied to FeBSs. For instance, QPI with vortex cores as scattering centers in principle can offer phase sensitive information, since vortices as magnetic scattering potentials can enhance the signal of certain scattering wave vectors (32). However, vortices are spatially more extended in FeBSs, which complicates comparison with theoretical calculations that assume point-like scattering potentials, making the interpretation of field-dependent QPI experiments disputed. Hereafter, new methods to visualize the symmetry of the SC gaps in FeBSs have been proposed. Among them, the method proposed by Hirschfeld, Altenfeld, Eremin, and Mazin (HAEM) is based on an integral over the real part of anti-symmetrized inter-pocket FT-QPI scattering pattern (43). Nevertheless, the original HAEM method requires one single impurity sited at the exact center in QPI mappings (31, 33). It is difficult to eliminate the irrelevant phase information when there are visibly multiple defects in the QPI mapping, although there have been investigations to do so (44). Another method, called defect-induced bound states QPI (DBS-QPI), extracts the scattering phase of FT-QPI at positive energy $\theta_{\mathbf{q},E}$ and negative energy $\theta_{\mathbf{q},-E}$, and using the phase difference $\theta_{\mathbf{q},-E} - \theta_{\mathbf{q},E}$ to offset phase coming from irrelevant details of defects (34, 45). Thus, the obtained DBS-QPI can clearly display phase information associated with SC gaps (46) (Supplementary Text 5.1). However, the DBS-QPI method is limited to the energies at defect-induced bound states. Even though later experiments used DBS-QPI method at the energies near the SC gap edge or within SC gap, these researches still rely on defect-induced bound states, which are supposed to appear near the gap edges and mix with the gap peaks (47), or produce a continuous change of density of states within the SC gap rather than generate sharp bound state peaks (48).

Here, we proposed a PR-QPI method, which adopts the data process in the DBS-QPI method. The PR-QPI signals at positive and negative energies are defined as

$$g_{pr}(\mathbf{q}, +E) = |g(\mathbf{q}, +E)| \cos(\theta_{\mathbf{q},+E} - \theta_{\mathbf{q},-E}) \quad (1)$$

$$g_{pr}(\mathbf{q}, -E) = |g(\mathbf{q}, -E)| \quad (2)$$

However, our PR-QPI method is based on the energy range between the gap maximum $|\Delta_2^{max}|$ and the gap minimum $|\Delta_2^{min}|$, which is different from the DBS-QPI method relied on defect-induced bound states. We thoroughly interpret our PR-QPI method in Supplementary Text 5.2. Briefly speaking, provided that the scattering potential is non-magnetic and relatively weak, $g_{pr}(\mathbf{q}, +E)$ should be negative for the scattering involving the sign-changed gaps and yet positive for the sign-preserved scattering vectors. Accordingly, if the gap signs on δ_2 and δ_1 are opposite, we are supposed to see negative-signal arcs in $g_{pr}(\mathbf{q}, +E)$ at the energy within $|\Delta_2^{min}|$ and $|\Delta_2^{max}|$, whereas $g_{pr}(\mathbf{q}, -E)$ is always positive according to the definition, which can be ignored.

We used our PR-QPI method to determine the relative gap sign in 1-UC Fe(Se,Te)/STO. Figure 4 shows the typical FT-QPI patterns $|g(\mathbf{q}, +E)|$ and corresponding PR-QPI patterns $g_{pr}(\mathbf{q}, +E)$ (see Fig. S12 for full PR-QPI patterns). We firstly focus on the pattern at $E = 18$ meV, i.e. the gap maximum.

One can see that the most contour of \mathbf{q}_1 ring (Fig. 4A, the central scattering ring) shows negative signals in the corresponding PR-QPI pattern (Fig. 4E, blue pixels), which clarifies two phenomenological questions of utmost importance. For one thing, the outer pocket δ_2 and the inner pocket δ_1 have opposite gap signs, indicating the sign reversal gap symmetry in 1-UC Fe(Se,Te)/STO. For the other, the intensity of inter-pocket scattering dominates over the \mathbf{q}_1 ring, which exactly benefits from the more coherent sign-changed scattering channel (see Supplementary Text 3.2 for discussion about Bogoliubov coherence factors). In addition, the intra-pocket scatterings of $\delta_1 \leftrightarrow \delta_1$ and $\delta_2 \leftrightarrow \delta_2$ naturally preserve the gap sign, producing the positive (albeit more fragile) signals in $g_{pr}(\mathbf{q}, +E)$, which are depicted as the red pixels inside and outside the blue pixel ring structure in Fig. 4E. Although the red-blue-red pixels along $\Gamma\tilde{M}$ directions are consistent with both ‘bonding-antibonding’ s_{\pm} -wave and ‘quasi-nodeless’ d -wave, the noticeably red pixels in $\Gamma\tilde{X}$ directions in Fig. 4E prefer ‘bonding-antibonding’ s_{\pm} -wave scenario to ‘quasi-nodeless’ d -wave scenario (see Fig. S13 for simulation results).

Then, we concentrate on the evolution of PR-QPI patterns as energy varies, which is supposed to follow the same trend as FT-QPI patterns (Fig. 4, A to D). As expected, the region where negative signals occupy gradually shrinks as energy decreases from 18 meV to 12 meV (Fig. 4, E to G), due to the contraction of the banana-shape CECs of δ_2 . Especially, at $E = 12$ meV, the negative signals only aggregate in small regions centered in $\Gamma\tilde{M}$ directions (Fig. 4G), where the signals slightly change to positive at $E = 11$ meV (Fig. S12). Eventually, the positive signals become conspicuous, completely covering the \mathbf{q}_1 ring at $E = 10$ meV (Fig. 4H), which is in accordance with the obtained gap minimum $|\Delta_2^{min}| \approx 10$ meV. In order to manifest the evolution more quantitatively, we use the same data processing procedure as Fig. 3C to extract the line cut of phase part ($\cos(\theta_{\mathbf{q},+E} - \theta_{\mathbf{q},-E})$) in PR-QPI pattern, and use the line cut to determine the sign of the maximum-intensity points in FT-QPI patterns (Fig. 3C, colored dots). The maximum-intensity points at energy within 18 meV and 14 meV have negative phase part in PR-QPI, while they have nearly vanishing phase part at energy within 13 meV and 11 meV, and finally have distinctly positive phase part at $E = 10$ meV. If the higher order terms in the \hat{T} -matrix approach cannot be neglected any more, i.e. approaching the ‘singularity’ in the \hat{T} -matrix, the sign-changed scattering would be weakened, possibly resulting in a reverse of the phase part. We discuss in Supplementary Text 5.2 the conditions under which the ‘singularity’ is not strong enough to change the sign of PR-QPI signals. Here, the positive signals at $E = 10$ meV originate from the intra-pocket scattering of $\delta_1 \leftrightarrow \delta_1$ instead of the ‘singularity’ effect (Fig. 4H).

Furthermore, the evolution of our PR-QPI signals from negative to positive as energy decreases can undoubtedly corroborate the gap sign change and the non-magnetic scattering potential simultaneously. For magnetic scattering potential, the gap-sign-changed scattering would present positive signals in PR-QPI patterns, while the gap-sign-preserved scattering would present negative signals (Supplementary Text 5.2). Therefore, if the two pockets share the same gap sign with magnetic scattering potential, the PR-QPI signal would always be negative as energy varies. Furthermore, provided the magnetic scattering potential on sign-changed gaps, the PR-QPI signals are supposed to change from positive to negative as energy decreases, which obviously contradicts our observation.

Finally, we analyze the \mathbf{q}_2 ring at $E = 18$ meV (Fig. 4A). The PR- \mathbf{q}_2 scattering pattern (Fig. 4E) shows the outer positive-signal arcs and the middle negative-signal arcs, verifying the sign reversal gaps on the two pockets, once again. However, compared to the \mathbf{q}_1 ring, the inner positive-signal arcs disappear, which may arise from two aspects. For one thing, while intra-orbital scatterings of $d_{xz} \leftrightarrow d_{xz}$ and $d_{yz} \leftrightarrow d_{yz}$ significantly contribute to the inner positive signals in \mathbf{q}_1 ring (note that the d orbital is

defined in 1-Fe unit cell, see Fig. S8 for the orbital character of FSs), inter-orbital scatterings of $d_{xz} \leftrightarrow d_{yz}$ normally are suppressed in FeBSs and have negligible effect on \mathbf{q}_2 ring (29, 30). For the other, the sign-preserved scatterings associated with the folded bands scarcely contribute to the scattering intensity either, due to the weak spectral weight. Thus, it is reasonable for the inner positive-signal arcs, which mainly consist of the inter-orbital scatterings of $d_{xz} \leftrightarrow d_{yz}$ and the scatterings associated with the folded bands, to be missing in PR- \mathbf{q}_2 scattering pattern (see Supplementary Text 3.1 for a thorough discussion of \mathbf{q}_2 ring).

Discussion

Combining the SC gap structure and gap sign, we could deduce the gap symmetry and the pairing mechanism of 1-UC Fe(Se,Te)/STO. For conventional superconductors, attractive interactions arising from electron-phonon coupling result in an s_{++} -wave state in which the SC gap sign is same everywhere in \mathbf{k} -space. Nevertheless, in high-temperature superconductors, the electron-phonon coupling is normally believed to be too weak for pairing (49) and strong on-site Coulomb repulsion demands the intra-orbital pairing (50) and a sign-change in \mathbf{k} -space, which favors an s_{\pm} -wave state (13) or a d -wave state (51) mediated by the exchange of quantum-order fluctuations, such as spin fluctuations (SF) (49). Regarding the FeBSs, it is widely accepted that, when the long-range antiferromagnetic (AFM) order of the parent compounds is suppressed (52), AFM-SF could act as pairing ‘glue’ to make superconductivity thrive, favoring an s_{\pm} -wave pairing symmetry, i.e. the order parameters have an opposite sign on the electron and hole pockets (53). However, in the 1-UC FeSe-based system, the electron doping makes the hole pocket below Fermi energy, leading to the question whether there still have sign reversal gaps between the electron pockets. By using PR-QPI method, we directly visualized the opposite SC gap signs on the two electron pockets, which fits into the picture of s_{\pm} -wave pairing symmetry.

As for ‘quasi-nodeless’ d -wave pairing symmetry, superconductivity also results from SF, and SC gap changes sign within the inner and outer pockets. Since the intra-orbital inter-pocket $d_{xy} \leftrightarrow d_{xy}$ pair scattering can take advantage of the major SF at (π, π) in the unfolded BZ (see Fig. S8 for the orbital character of FSs), the SC gap is supposed to be maximum at the tip of the elliptic-shaped pockets where the d_{xy} orbital has largest weight (54). However, this naturally generates the gap maximum in the $\Gamma\tilde{M}$ direction (in the folded BZ) and gap minimum, albeit not zero, in the $\Gamma\tilde{X}$ direction, where the two ellipses crossed (19), which fully conflicts with our determination of gap maximum in the $\Gamma\tilde{X}$ direction and gap minimum in the $\Gamma\tilde{M}$ direction (Fig. 3D). It is argued that the electron correlations of d_{xy} bands are significantly stronger than that of d_{xz}/d_{yz} bands in many FeBSs (55, 56). This orbital-selective electron correlations shall induce orbital-selective SC pairing, which relatively strengthens the inter-orbital ($d_{xz} \leftrightarrow d_{yz}$) pairing (54), and accordingly increases the SC gap in the $\Gamma\tilde{X}$ direction. However, even considering the orbital-selective pairing, the SC gap on the d_{xy} orbital is still supposed to be larger than the SC gap on the d_{xz}/d_{yz} orbitals in the 1-UC FeSe-based system (8, 54). In our experiment, the gap maximum lies in the $\Gamma\tilde{X}$ direction, where the d_{xy} orbital component is supposed to have less weight (54). Thus, the conflict cannot be solved solely by orbital-selective pairing, and the ‘quasi-nodeless’ d -wave seems to be inconsistent with our results.

In the microscopic theory of superconductivity, the scattering of electron pairs from $(\mathbf{k}, -\mathbf{k})$ to $(\mathbf{k}', -\mathbf{k}')$ will contribute to the formation of the Cooper pairs, and the condensation of these Cooper pairs will lead to superconductivity. After that, not only a low-energy SC gap $\Delta(\mathbf{k})$ opens to prevent the breaking of Cooper pairs, but also the band dispersion at a higher-energy range can be modified by the

self-energy effect originating from the pairing interaction especially like electron-boson coupling (41). This higher-energy band renormalization offers an alternative method to identify the pairing interaction and reveal the pairing mechanism. We also performed QPI measurements in 1-UC FeSe/STO at this higher-energy range (57). It is shown that the band dispersion extracted from the FT-QPI patterns is heavily renormalized in the $\Gamma\tilde{X}$ direction at $E = 37$ meV, coinciding in the bosonic mode energy detected in the tunneling spectrum, whereas this dispersion renormalization is moderate in the $\Gamma\tilde{M}$ direction. This result once again confirms that the electron pairs in the $\Gamma\tilde{X}$ direction generate a larger SC gap and a stronger band renormalization at the same time. We noticed that upon increasing the band hybridization of the two elliptic-shaped electron pockets, the interplay between intra-pocket and inter-pocket pairings will transform the system from a d -wave state to an s_{\pm} -wave state, where the location of the gap maximum simultaneously transforms from $\Gamma\tilde{M}$ direction to $\Gamma\tilde{X}$ direction (17). This proposal supports the ‘bonding-antibonding’ s_{\pm} -wave scenarios as the pairing symmetry and qualitatively matches the gap structure we extracted.

Widely discussed ingredients for topological superconductors are (i) unconventional pairing in multiband systems and (ii) SOC. This work directly unravels the nature of the SC order parameter in showing that it is unconventional (with sign change). Overall, both the gap sign change and the gap structure in 1-UC Fe(Se,Te)/STO are well consistent with the ‘bonding-antibonding’ s_{\pm} -wave pairing symmetry, indicating a unified picture of pairing in FeBSs. The ‘bonding-antibonding’ s_{\pm} -state can be driven by SF in conjunction with hybridization of the electron pockets from SOC, thus our work also gives valuable input for further understanding of whether and how topological superconductivity can be realized in FeBSs.

Materials and Methods

Sample synthesis. Our experiments were performed in an ultrahigh-vacuum ($\sim 2 \times 10^{-10}$ mbar) MBE-STM combined system (Scienta Omicron). The Nb-doped SrTiO₃(001) (wt 0.7 %) substrates were thermally boiled in 90 °C deionized water for 50 minutes and then chemically etched in 10% HCl for 45 minutes. Followed by Se-flux method in MBE chamber, the substrates finally obtain the atomically flat TiO₂-terminated surface. The 1-UC Fe(Se,Te) films were grown by co-evaporating high-purity Fe (99.994%) Se (99.999%) and Te (99.999%), with the substrates held at 340 °C. Then the as-grown 1-UC Fe(Se,Te) films were annealed at 380 °C for 3 hours.

STM/STS measurements. All STM/STS data were acquired in the *in-situ* STM chamber with a polycrystalline Pt/Ir tip by using the standard lock-in technique. The modulation voltage $V_{\text{mod}} = 0.5$ mV at 1.7699 kHz. The setup of STM topographic images is $V = 0.1$ V, $I = 0.5$ nA unless specified. And the setup of all STS measurements is $V = 0.04$ V, $I = 2.5$ nA for tunneling spectra and differential conductance mapping, i.e. QPI. All STM/STS measurements were taken at 4.3 K. The energy resolution of all STS measurements is $\Delta E = \sqrt{(3.5k_{\text{B}}T)^2 + (2.5eV_{\text{mod}})^2} = 1.8$ meV, where k_{B} is Boltzmann constant.

Data availability. All study data are included in the article and/or supporting information.

ACKNOWLEDGMENTS. The authors acknowledge the discussions with Brian M. Andersen and Peter J. Hirschfeld. This work was financially supported by National Natural Science Foundation of China (No.11888101), National Key R&D Program of China (No. 2018YFA0305604), Beijing Natural

Science Foundation (No. Z180010), and Strategic Priority Research Program of Chinese Academy of Sciences (No. XDB28000000).

References

1. Q. Y. Wang *et al.*, Interface-induced high-temperature superconductivity in single unit-cell FeSe films on SrTiO₃. *Chin. Phys. Lett.* **29**, 037402 (2012).
2. W. H. Zhang *et al.*, Direct observation of high-temperature superconductivity in one-unit-cell FeSe films. *Chin. Phys. Lett.* **31**, 017401 (2014).
3. S. L. He *et al.*, Phase diagram and electronic indication of high-temperature superconductivity at 65 K in single-layer FeSe films. *Nat. Mater.* **12**, 605-610 (2013).
4. S. Y. Tan *et al.*, Interface-induced superconductivity and strain-dependent spin density waves in FeSe/SrTiO₃ thin films. *Nat. Mater.* **12**, 634-640 (2013).
5. C. Liu *et al.*, Extensive impurity-scattering study on the pairing symmetry of monolayer FeSe films on SrTiO₃. *Phys. Rev. B* **97**, 024502 (2018).
6. D. F. Liu *et al.*, Electronic origin of high-temperature superconductivity in single layer FeSe superconductor. *Nat. Commun.* **3**, 931 (2012).
7. J. J. Lee *et al.*, Interfacial mode-coupling as the origin of the enhancement of T_C in FeSe films on SrTiO₃. *Nature* **515**, 245-248 (2014).
8. Y. Zhang *et al.*, Superconducting gap anisotropy in monolayer FeSe thin film. *Phys. Rev. Lett.* **117**, 117001 (2016).
9. P. J. Hirschfeld, M. M. Korshunov, I. I. Mazin, Gap symmetry and structure of Fe-based superconductors. *Rep. Prog. Phys.* **74**, 124508 (2011).
10. C. F. Liu, J. Wang, Heterostructural one-unit-cell FeSe/SrTiO₃: from high-temperature superconductivity to topological states. *2D Mater.* **7**, 022006 (2020).
11. R. M. Fernandes *et al.*, Iron pnictides and chalcogenides: a new paradigm for superconductivity. *Nature* **601**, 35-44 (2022).
12. D. Huang *et al.*, Revealing the empty-state electronic structure of single-unit-cell FeSe/SrTiO₃. *Phys. Rev. Lett.* **115**, 017002 (2015).
13. I. I. Mazin, D. J. Singh, S. M. Johannes, M. H. Du, Unconventional superconductivity with a sign reversal in the order parameter of LaFeAsO_{1-x}F_x. *Phys. Rev. Lett.* **101**, 057003 (2008).
14. Y. Yamakawa, H. Kontani, Superconductivity without a hole pocket in electron-doped FeSe: Analysis beyond the Migdal-Eliashberg formalism. *Phys. Rev. B* **96**, 045130 (2017).
15. J. Kang, R. M. Fernandes, Superconductivity in FeSe thin films driven by the interplay between nematic fluctuations and spin-orbit coupling. *Phys. Rev. Lett.* **117**, 217003 (2016).
16. I. I. Mazin, Symmetry analysis of possible superconducting states in K_xFe_ySe₂ superconductors. *Phys. Rev. B* **84**, 024529 (2011).
17. M. Khodas, A. V. Chubukov, Interpocket pairing and gap symmetry in Fe-based superconductors with only electron pockets. *Phys. Rev. Lett.* **108**, 247003 (2012).
18. K. Kuroki *et al.*, Unconventional pairing originating from the disconnected Fermi surfaces of superconducting LaFeAsO_{1-x}F_x. *Phys. Rev. Lett.* **101**, 087004 (2008).
19. D. F. Agterberg, T. Shishidou, J. O'Halloran, P. M. R. Brydon, M. Weinert, Resilient nodeless d-wave superconductivity in monolayer FeSe. *Phys. Rev. Lett.* **119**, 267001 (2017).
20. Q. Fan *et al.*, Plain s-wave superconductivity in single-layer FeSe on SrTiO₃ probed by scanning tunnelling microscopy. *Nat. Phys.* **11**, 946-952 (2015).

21. C. F. Liu *et al.*, Spectroscopic Imaging of Quasiparticle Bound States Induced by Strong Nonmagnetic Scatterings in One-Unit-Cell FeSe/SrTiO₃. *Phys. Rev. Lett.* **123**, 036801 (2019).
22. X. X. Wu, S. S. Qin, Y. Liang, H. Fan, J. P. Hu, Topological characters in Fe(Te_{1-x}Se_x) thin films. *Phys. Rev. B* **93**, 115129 (2016).
23. X. X. Wu, X. Liu, R. Thomale, C. X. Liu, High- T_c superconductor Fe(Se,Te) monolayer: an intrinsic, scalable and electrically tunable Majorana platform. *Natl. Sci. Rev.* **9**, nwab087 (2022).
24. X. L. Peng *et al.*, Observation of topological transition in high- T_c superconducting monolayer FeTe_{1-x}Se_x films on SrTiO₃ (001). *Phys. Rev. B* **100**, 155134 (2019).
25. F. S. Li *et al.*, Interface-enhanced high-temperature superconductivity in single-unit-cell FeTe_{1-x}Se_x films on SrTiO₃. *Phys. Rev. B* **91**, 220503 (2015).
26. C. Chen *et al.*, Atomic line defects and zero-energy end states in monolayer Fe (Te, Se) high-temperature superconductors. *Nat. Phys.* **16**, 536-540 (2020).
27. Y. Zhang, K. Jiang, F. Zhang, J. Wang, Z. Wang, Atomic line defects and topological superconductivity in unconventional superconductors. *Phys. Rev. X* **11**, 011041 (2021).
28. Q. H. Wang, D. H. Lee, Quasiparticle scattering interference in high-temperature superconductors. *Phys. Rev. B* **67**, 020511 (2003).
29. Y. Y. Zhang *et al.*, Quasiparticle scattering interference in superconducting iron pnictides. *Phys. Rev. B* **80**, 094528 (2009).
30. M. P. Allan *et al.*, Anisotropic energy gaps of iron-based superconductivity from intraband quasiparticle interference in LiFeAs. *Science* **336**, 563-567 (2012).
31. P. O. Sprau *et al.*, Discovery of orbital-selective Cooper pairing in FeSe. *Science* **357**, 75-80 (2017).
32. T. Hanaguri, S. Niitaka, K. Kuroki, H. Takagi, Unconventional s-wave superconductivity in Fe(Se,Te). *Science* **328**, 474-476 (2010).
33. Z. Y. Du *et al.*, Sign reversal of the order parameter in (Li_{1-x}Fe_x)OHFe_{1-y}Zn_ySe. *Nat. Phys.* **14**, 134-139 (2018).
34. S. Chi *et al.*, Determination of the superconducting order parameter from defect bound state quasiparticle interference. arXiv: 1710.09089.
35. Z. Y. Wang *et al.*, Close relationship between superconductivity and the bosonic mode in Ba_{0.6}K_{0.4}Fe₂As₂ and Na(Fe_{0.975}Co_{0.025})As. *Nat. Phys.* **9**, 42-48 (2013).
36. C. Chen, C. F. Liu, Y. Liu, J. Wang, Bosonic Mode and Impurity-Scattering in Monolayer Fe(Se,Te) High-Temperature Superconductors. *Nano Lett.* **20**, 2056-2061 (2020).
37. R. C. Dynes, V. Narayanamurti, J. P. Garno, Direct measurement of quasiparticle-lifetime broadening in a strong-coupled superconductor. *Phys. Rev. Lett.* **41**, 1509-1512 (1978).
38. R. C. Dynes, J. P. Garno, G. B. Hertel, T. P. Orlando, Tunneling study of superconductivity near the metal-insulator transition. *Phys. Rev. Lett.* **53**, 2437-2440 (1984).
39. M. J. Lawler *et al.*, Intra-unit-cell electronic nematicity of the high- T_c copper-oxide pseudogap states. *Nature* **466**, 347-351 (2010).
40. D. Huang *et al.*, Bounds on nanoscale nematicity in single-layer FeSe/SrTiO₃. *Phys. Rev. B* **93**, 125129 (2016).
41. M. P. Allan *et al.*, Identifying the fingerprint of antiferromagnetic spin fluctuations in iron pnictide superconductors. *Nat. Phys.* **11**, 177-182 (2015).
42. Z. Y. Du *et al.*, Scrutinizing the double superconducting gaps and strong coupling pairing in (Li_{1-x}Fe_x)OHFeSe. *Nat. Commun.* **7**, 10565 (2016).
43. P. J. Hirschfeld, D. Altenfeld, I. Eremin, I. I. Mazin, Robust determination of the superconducting gap sign

- structure via quasiparticle interference. *Phys. Rev. B* **92**, 184513 (2015).
44. R. Sharma *et al.*, Multi-atom quasiparticle scattering interference for superconductor energy-gap symmetry determination. *npj Quantum Mater.* **6**, 1-7 (2021).
 45. S. Chi *et al.*, Extracting phase information about the superconducting order parameter from defect bound states. arXiv: 1710.09088.
 46. Q. Q. Gu *et al.*, Sign-reversal superconducting gaps revealed by phase-referenced quasiparticle interference of impurity-induced bound states in $(\text{Li}_{1-x}\text{Fe}_x)\text{OHFe}_{1-y}\text{Zn}_y\text{Se}$. *Phys. Rev. B* **98**, 134503 (2018).
 47. M. Y. Chen *et al.*, Direct visualization of sign-reversal s_{\pm} superconducting gaps in $\text{FeTe}_{0.55}\text{Se}_{0.45}$. *Phys. Rev. B* **99**, 014507 (2019).
 48. Q. Q. Gu *et al.*, Directly visualizing the sign change of d -wave superconducting gap in $\text{Bi}_2\text{Sr}_2\text{CaCu}_2\text{O}_{8+\delta}$ by phase-referenced quasiparticle interference. *Nat. Commun.* **10**, 1603 (2019).
 49. D. J. Scalapino, A common thread: The pairing interaction for unconventional superconductors. *Rev. Mod. Phys.* **84**, 1383-1417 (2012).
 50. A. Chubukov, Pairing mechanism in Fe-based superconductors. *Annu. Rev. Con. Mat. Phys.* **3**, 57-92 (2012).
 51. C. C. Tsuei, J. R. Kirtley, Pairing symmetry in cuprate superconductors. *Rev. Mod. Phys.* **72**, 969-1016 (2000).
 52. C. de La Cruz *et al.*, Magnetic order close to superconductivity in the iron-based layered $\text{LaO}_{1-x}\text{F}_x\text{FeAs}$ systems. *Nature* **453**, 899-902 (2008).
 53. F. Wang, D. H. Lee, The electron-pairing mechanism of iron-based superconductors. *Science* **332**, 200-204 (2011).
 54. A. Kreisel *et al.*, Orbital selective pairing and gap structures of iron-based superconductors. *Phys. Rev. B* **95**, 174504 (2017).
 55. M. Yi *et al.*, Observation of universal strong orbital-dependent correlation effects in iron chalcogenides. *Nat. Commun.* **6**, 7777 (2015).
 56. Z. P. Yin, K. Haule, G. Kotliar, Kinetic frustration and the nature of the magnetic and paramagnetic states in iron pnictides and iron chalcogenides. *Nat. Mater.* **10**, 932-935 (2011).
 57. C. F. Liu *et al.*, Orbital-Selective High-Temperature Cooper Pairing Developed in the Two-Dimensional Limit. *Nano Lett.* **22**, 3245-3251 (2022).

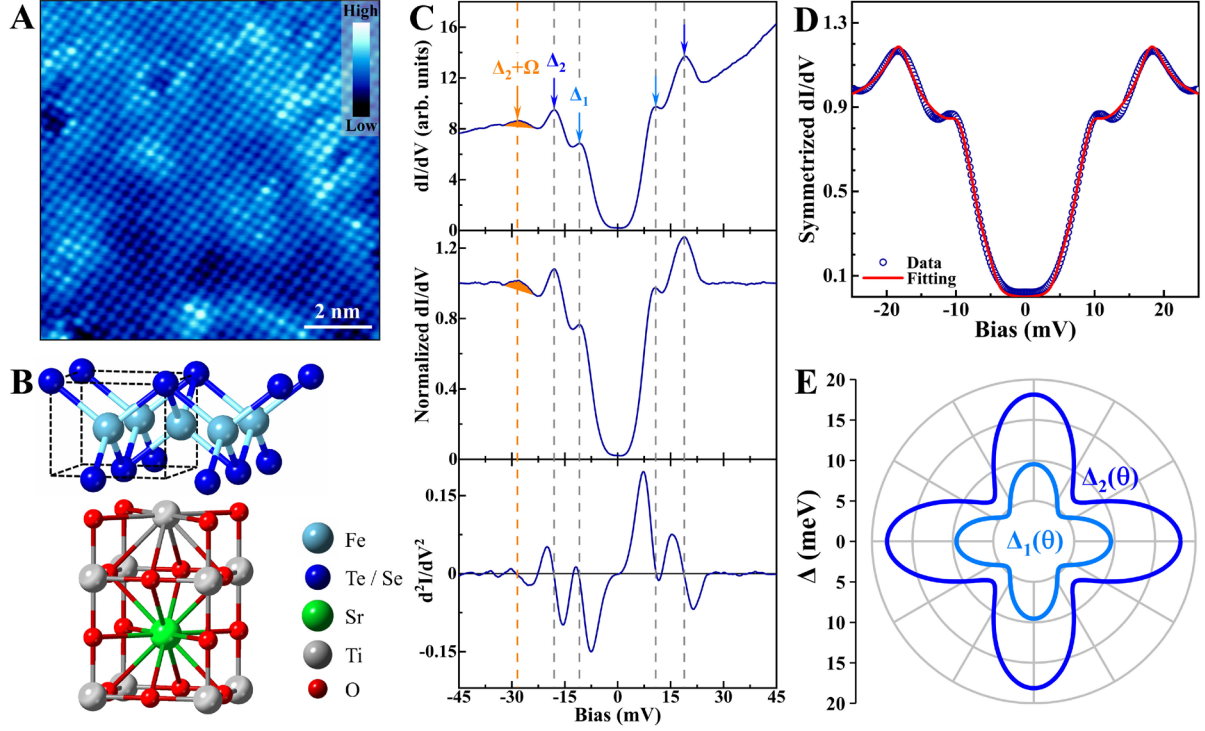


Fig. 1. STM topography and SC gap anisotropy revealed by Dynes model fittings in 1-UC Fe(Se,Te)/STO. (A) STM topographic image ($10 \times 10 \text{ nm}^2$) showing the topmost Se/Te lattice. (B) Crystal structure of 1-UC Fe(Se,Te)/STO. The dashed black box indicates 2-Fe UC. (C) Typical tunneling spectra showing raw dI/dV (top panel), normalized dI/dV (middle panel), and second derivative of conductance d^2I/dV^2 (bottom panel) at 4.3 K. The gray and orange dashed lines show the approximate energies of $|\Delta_1| = -11.1 \text{ meV} / 11.0 \text{ meV}$, $|\Delta_2| = -18.2 \text{ meV} / 18.8 \text{ meV}$ and $|\Delta_2| + \Omega = -28.2 \text{ meV}$, and the orange areas highlight the hump features developing from the bosonic mode Ω . The normalization was performed by dividing the raw dI/dV spectrum by its polynomial background, which was obtained by a cubic fitting to the raw dI/dV spectrum for $|V| \geq 30 \text{ mV}$. (D) Symmetrized dI/dV spectrum (blue hollow dots). The particle-hole symmetrization was realized by averaging the negative bias side and the positive bias side of the normalized dI/dV spectrum. The red solid line is the theoretical fitting by two-band anisotropic Dynes model. (E) Anisotropic gap functions used in the fitting.

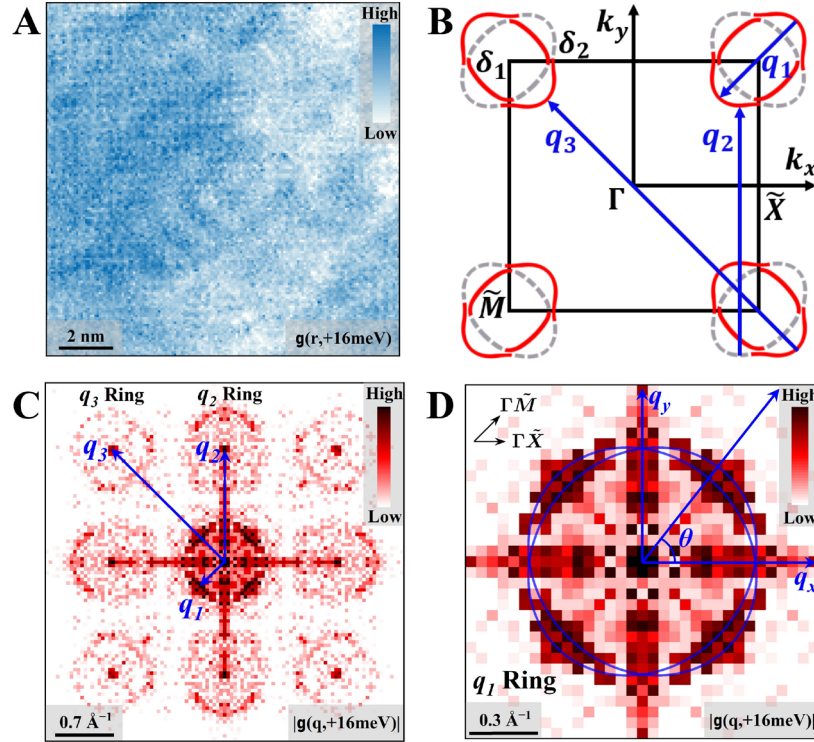


Fig. 2. QPI and FT-QPI patterns. (A) Differential conductance mapping $g(r, E = 16 \text{ meV})$ (4.3 K, $13 \times 13 \text{ nm}^2$) after distortion-correction, showing the interference patterns. (B) The schematic FSs of 1-UC Fe(Se,Te)/STO in 2-Fe BZ. The red solid ellipses and gray dashed ellipses both denote the electron pockets, while the latter have weaker spectral weight. After band hybridization, the initial elliptic-shaped electron pockets form the inner pockets δ_1 and outer pockets δ_2 . The blue solid lines q_1 , q_2 and q_3 show the representative scattering vectors corresponding to the scattering vectors in (C). The k_x/k_y coordinate system also correlates with the q_x/q_y coordinate system in (D). (C) FT-QPI pattern of $|g(q, E = 16 \text{ meV})|$ after symmetrization and Gaussian core subtraction shows three types of scattering patterns. We use q_1 , q_2 and q_3 rings to denote the corresponding scattering patterns. (D) Zoom-in image of the central part of (C) to clearly show q_1 ring. The blue solid ellipses are schematically plotted to roughly outline the contour and the angle θ is defined relative to q_x .

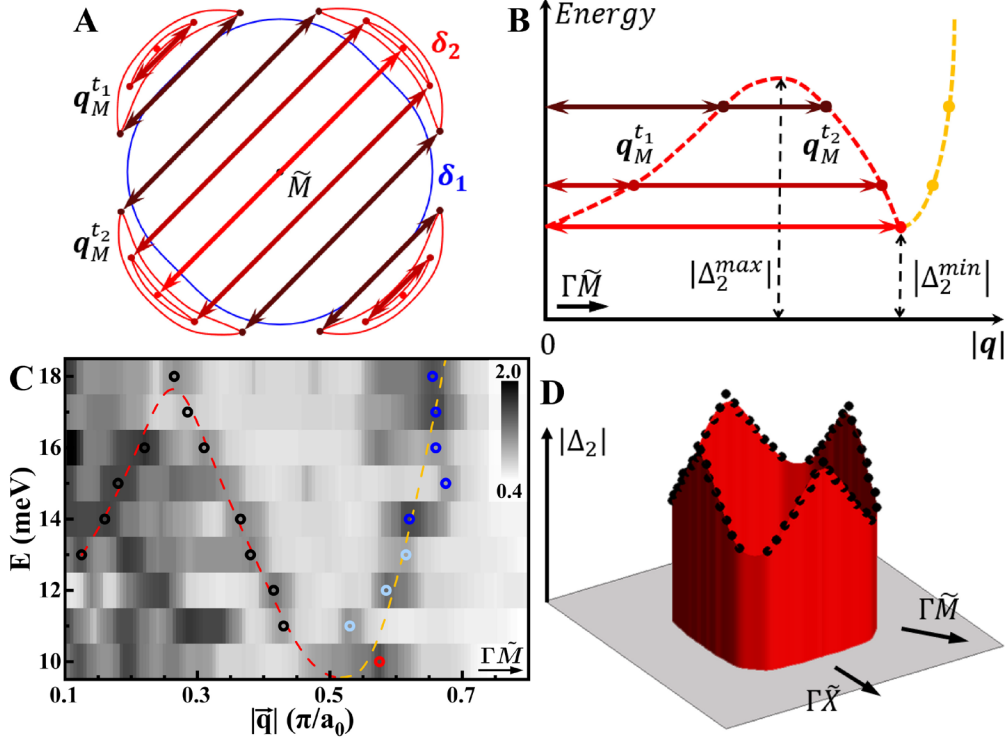


Fig. 3. Anisotropic SC gap extracted from central FT-QPI pattern. (A) Schematic CECs of Bogoliubov quasiparticles (red contours) for δ_2 at \tilde{M} in the folded BZ. The anisotropic gap is C_4 symmetric with maximum in the $\Gamma\tilde{X}$ directions ($\theta = 0^\circ + 90^\circ \times N$) and minimum in the $\Gamma\tilde{M}$ directions ($\theta = 45^\circ + 90^\circ \times N$). As energy increases, the size of CECs enlarges, and the tips of CECs are emphasized by the red dots with gradually darkened color. Correspondingly, the arrows with gradually darkened color depict the scatterings vectors associated with ‘banana’ tips along a high symmetry direction at $\theta = 45^\circ$ ($\Gamma\tilde{M}$). The blue contour represents the schematic FS of δ_1 . (B) The schematic curved shape in a $|\mathbf{q}|-E$ plot. The red dashed curve, coming from the scattering vectors in **a** (shorter arrows $\mathbf{q}_M^{t_1}$ and longer arrows $\mathbf{q}_M^{t_2}$), reflects the anisotropic gap structure. The orange dashed curve shows the band dispersion $E(\mathbf{q}) = E(2\mathbf{k})$, deriving from the evolution of the banana-shaped contours at $\theta = 45^\circ$ rather than the extension of the ‘banana’ tips. (C) Intensity plot in a $|\mathbf{q}|-E$ plane where line cuts are along $\theta = 45^\circ$. The black and colored hollow dots locate the maximum-intensity points associated with ‘banana’ tips and opposite-side scatterings $\mathbf{k} \leftrightarrow -\mathbf{k}$, respectively. The color of the dots indicates the sign in their corresponding PR-QPI pattern (Fig. 4) with blue denoting negative, light blue denoting almost zero, and red denoting positive. The red and orange dashed curves schematically depict the trajectories of the maximum-intensity points, qualitatively matching the curves in (B). (D) The \mathbf{k} -space structure of the SC gap (black solid dots) and FS, simultaneously obtained by (C).

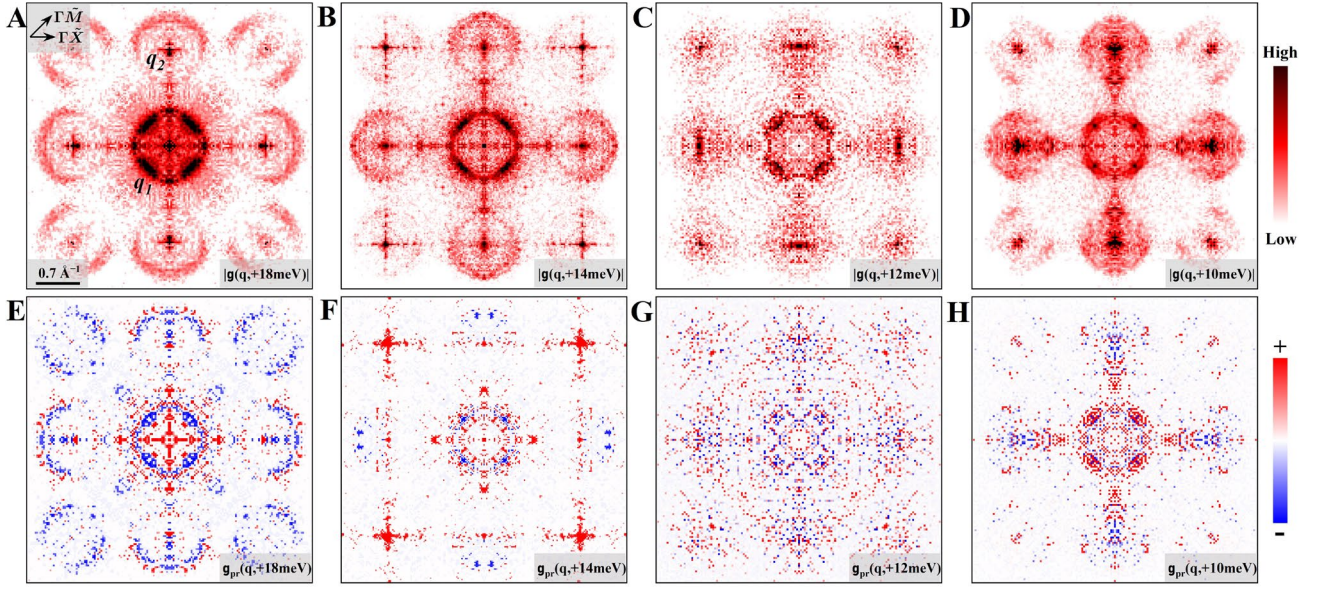


Fig. 4. The typical FT-QPI patterns $|g(\mathbf{q}, +E)|$ (A to D) and corresponding PR-QPI patterns $g_{pr}(\mathbf{q}, +E)$ (E to H). As the size of CECs of δ_2 gradually shrinks with decreasing energy from 18 meV to 10 meV, the sign-changed scattering signals (blue pixels of the central scattering ring \mathbf{q}_1 in (E to H)) constantly diminish and finally disappear.

Supplementary Information for

Anisotropic gap structure and sign reversal symmetry in monolayer Fe(Se,Te)

Yu Li^a, Dingyu Shen^a, Andreas Kreisel^b, Cheng Chen^a, Tianheng Wei^a, Xiaotong Xu^a & Jian Wang^{a,c,d,e,1}

^aInternational Center for Quantum Materials, School of Physics, Peking University, Beijing 100871, China.

^bInstitut für Theoretische Physik, Universität Leipzig, D-04103 Leipzig, Germany.

^cCollaborative Innovation Center of Quantum Matter, Beijing 100871, China.

^dCAS Center for Excellence in Topological Quantum Computation, University of Chinese Academy of Sciences, Beijing 100190, China.

^eBeijing Academy of Quantum Information Sciences, Beijing 100193, China.

¹To whom correspondence may be addressed. Email: jianwangphysics@pku.edu.cn.

This PDF file includes:

Supplementary Text

Figures S1 to S13

SI References

Supplementary Text

1. More Information about the One Unit-cell (1-UC) Fe(Se,Te)/STO and Dynes Model Fitting

1.1. 1-UC Fe(Se,Te)/STO Characterization

We used the thickness of the 2nd-UC Fe(Se,Te) film to estimate the Se content. Empirically, the thickness of the 2nd-UC Fe(Se,Te) is about 0.59 nm when Se concentration equals 50%^[1]. In order to verify the universality of the anisotropic gap structure in 1-UC Fe(Se,Te), we averaged over 180 spectra to represent a general tunneling spectrum (Fig. S1c) and tested the performance of the two-band anisotropic Dynes fittings on this general spectrum (Fig. S1d and S1e). Once again, the Dynes model exhibits excellent fittings and appropriate parameters of $|\Delta_1| = 9.65 \pm 0.25$ meV and $|\Delta_2| = 16.91 \pm 0.11$ meV. The gap values also moderately decrease, compared to those determined by d^2I/dV^2 ($|\Delta_1| = 11.9 \pm 0.1$ meV and $|\Delta_2| = 18$ meV). Accordingly, the scattering rates of $\Gamma_1 = 1.54 \pm 0.12$ meV and $\Gamma_2 = 2.52 \pm 0.07$ meV are relatively large, owing to both thermal broadening and average broadening. This larger broadening is also clearly manifested by the disappearance of coherence peaks of $|\Delta_1|$ and the emergence of a pair of kinks instead (Fig. S1e).

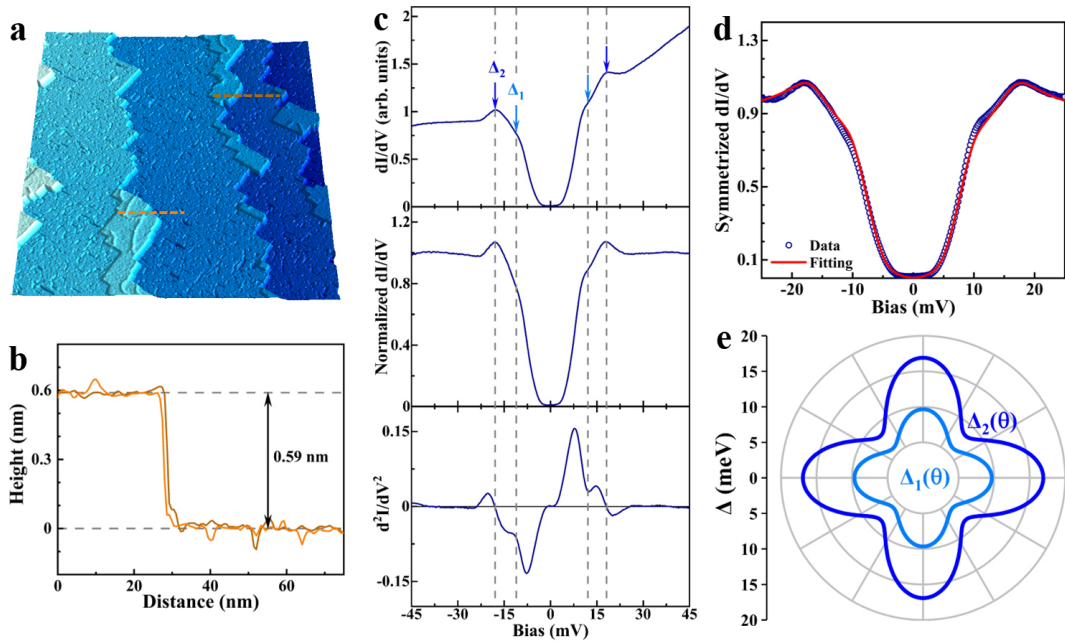


Figure S1. Scanning tunneling microscopy (STM) topography and tunneling spectra in 1-UC Fe(Se,Te)/STO.

a, The large-scale STM topography of 1-2 UC Fe(Se,Te)/STO (300×300 nm², $V = 1$ V, $I = 0.5$ nA), where the lighter color means the higher height. Apart from the terraces inherited from the STO substrate, the 2nd-UC Fe(Se,Te) film normally grows on the edge of the lower terrace. **b**, Profile taken along the orange and brown curves in **a**, respectively, both showing the thickness of the 2nd-UC Fe(Se,Te) film is 0.59 nm. Since the thickness of the 2nd-UC Fe(Se,Te) film changes with the ratio of Se/Te, height of 0.59 nm indicates the Se concentration is around 50%^[1]. **c**, An averaged (over 180 spectra) tunneling spectrum at 4.3 K, followed the same data processing procedure as Fig. 1c. The gray dashed lines show the approximate energies of $\Delta_1 = -11.8$ meV / 12 meV, $\Delta_2 = -18$ meV / 18 meV. **d**, The symmetrized dI/dV spectrum (blue hollow dots) fitted by the two-band anisotropic Dynes model (red solid line), with the anisotropic gap functions shown in **e**.

1.2. Comparison of Different Types of Dynes Model

Figure S2 and Figure S3 show the Dynes model fitting results of the individual tunneling spectrum and the averaged tunneling spectrum, respectively. We compared four different types of Dynes model and defined a quantity $e = \sqrt{\sum \delta y^2}$ to describe the goodness of every fit, where δy is the residual error. The simplest form is the original Dynes model^{[2],[3]} also named one-band isotropic Dynes model.

$$\frac{dI}{dV}(eV) = N(E_F) \frac{1}{k_B T} \int_{-\infty}^{+\infty} dE Re \left[\frac{|E-i\Gamma|}{\sqrt{(E-i\Gamma)^2 - \Delta^2}} \right] \cosh^{-2} \frac{E+eV}{2k_B T} \quad (1)$$

Here, $N(E_F)$ is the local density of states (DOSs) at E_F , Γ is the scattering rate, and k_B is the Boltzmann constant. Obviously, the one-band isotropic Dynes model cannot fit the tunneling spectrum (Fig. S2a) with an abnormally large $e = 1.13$ and only gives a single superconducting (SC) gap $|\Delta| = 8.58$ meV.

The fitting incorporating anisotropic gap structure (Fig. S2b) has a significant improvement compared to the isotropic gap fitting, where e dramatically decreases to 0.42 and the fitting parameter $|\Delta_2^{max}| = 18.17$ meV is comparable to the energy of the large coherence peaks (18.5 meV). The fitting functions are given by

$$\frac{dI}{dV} = N(E_F) \frac{1}{2\pi} \frac{1}{k_B T} \int_{-\infty}^{+\infty} dE \int_0^{2\pi} d\theta Re \left[\frac{|E-i\Gamma|}{\sqrt{(E-i\Gamma)^2 - \Delta(\theta)^2}} \right] \cosh^{-2} \frac{E+eV}{2k_B T} \quad (2)$$

$$\Delta(\theta) = \Delta^{max} [1 - p_1(1 - \cos 4\theta) - p_2(1 - \cos 2\theta)] \quad (3)$$

where the anisotropic function was adopted on account of its consistency with angle-resolved photoemission spectroscopy (ARPES) measurements of the angular-dependent $\Delta(\theta)$ in 1-UC FeSe^[4], and the ability to give the second maximum at $\theta = 90^\circ / 270^\circ$. This second maximum indeed corresponds to the small SC gap $|\Delta_1^{max}| = 9.09$ meV. However, it is moderately less than the energy of the small coherence peak (11 meV), also shown as the observable deviation between the fitting curve and the tunneling spectrum in Fig. S2b.

Next, we used the summation of two Dynes functions with different weights (w vs. $1-w$) to represent the two-band model, given by

$$\frac{dI}{dV} = N(E_F) \left[w \frac{dI_1}{dV} + (1-w) \frac{dI_2}{dV} \right] \quad (4)$$

Though the two-band isotropic Dynes model (Fig. S2c) fits the tunneling spectrum well ($e = 0.27$), the obtained parameters of $|\Delta_1| = 7.87$ meV and $|\Delta_2| = 16.46$ meV are unreasonably small, coming from the unusually large scattering rates of $\Gamma_1 = 2.41$ meV and $\Gamma_2 = 1.31$ meV.

After including gap anisotropy, two-band anisotropic Dynes model (Fig. S2d) displays the best fitting performance with lowest $e = 0.26$ and gives the most reasonable fitting parameter of $|\Delta_1^{max}| = 9.55$ meV, $|\Delta_2^{max}| = 18.13$ meV, $\Gamma_1 = 0.51$ meV, and $\Gamma_2 = 0.79$ meV, where the anisotropic function is given by

$$\Delta_{1/2}(\theta) = \Delta_{1/2}^{max} [1 - p_{1/2}(1 - \cos 4\theta)] \quad (5)$$

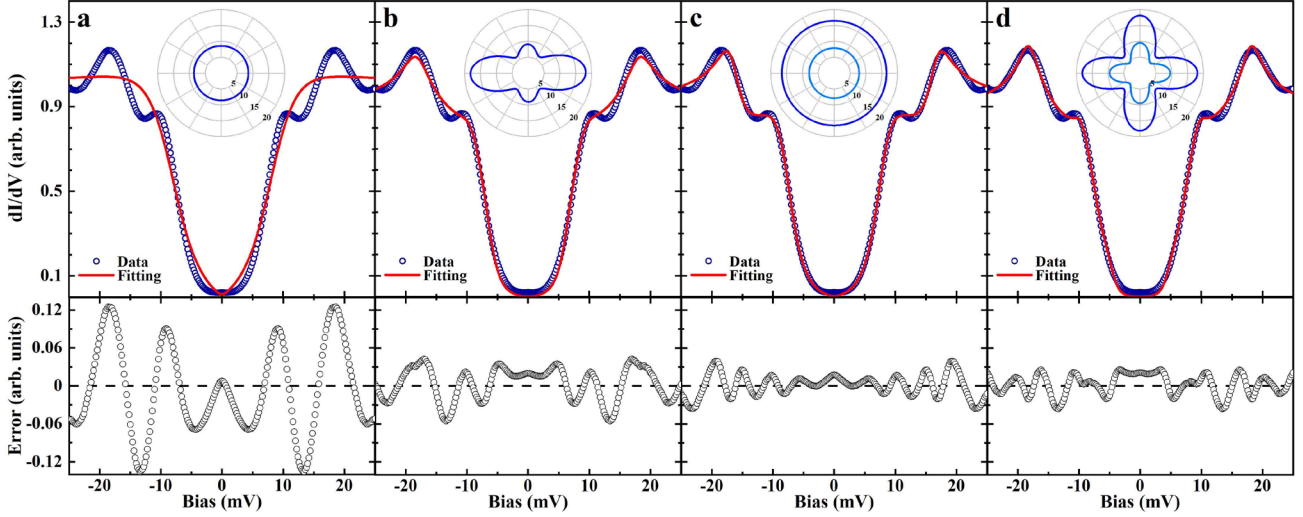


Figure S2. Fittings of the individual tunneling spectrum with different types of Dynes model. In the top panel, the blue hollow dots represent the symmetrized dI/dV spectrum and the red solid line is the theoretical fittings by different types of Dynes model. Inset shows the gap functions used in each Dynes model. Bottom panel shows the residual error defined as the symmetrized dI/dV spectrum subtracting the fitted curve. **a**, One-band isotropic Dynes model fitting. Fitting parameters: $|\Delta| = 8.58$ meV, $\Gamma = 5.12$ meV. Fitting error: $e = 1.13$. **b**, One-band anisotropic Dynes model fitting. $|\Delta_1| = 9.09$ meV, $|\Delta_2| = 18.17$ meV, $\Gamma = 1.28$ meV, $e = 0.42$. **c**, Two-band isotropic Dynes model fitting. $|\Delta_1| = 7.87$ meV, $|\Delta_2| = 16.46$ meV, $\Gamma_1 = 2.41$ meV, $\Gamma_2 = 1.31$ meV, $e = 0.27$. **d**, Two-band anisotropic Dynes model fitting. $|\Delta_1| = 9.55$ meV, $|\Delta_2| = 18.13$ meV, $\Gamma_1 = 0.51$ meV, $\Gamma_2 = 0.79$ meV, $e = 0.26$.

The fittings of the averaged tunneling spectrum further confirms that the two-band isotropic Dynes model provides unreasonable parameters, and two-band anisotropic Dynes model gives the best fitting (Fig. S3). One tiny difference in this case is that the one-band anisotropic Dynes model shows almost the same results with two-band anisotropic Dynes model. Overall, whether one-band or two-band, incorporating anisotropic gap functions dramatically promotes the performance of Dynes model, revealing the significance of SC gap anisotropy.

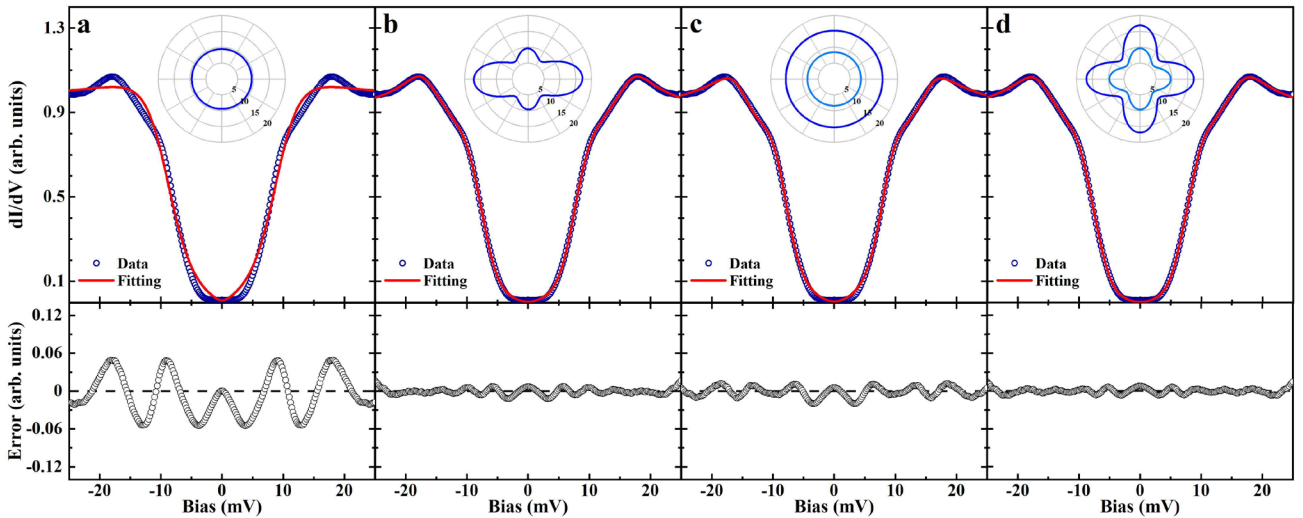


Figure S3. Fittings of the averaged tunneling spectrum with different types of Dynes model. Same data processing as Fig. S2 but for the averaged spectrum. **a**, One-band isotropic Dynes model fitting. Fitting parameters:

$|\Delta| = 9.44$ meV, $\Gamma = 4.77$ meV. Fitting error: $e = 0.52$. **b**, One-band anisotropic Dynes model fitting. $|\Delta_1| = 9.64$ meV, $|\Delta_2| = 17.12$ meV, $\Gamma = 2.23$ meV, $e = 0.08$. **c**, Two-band isotropic Dynes model fitting. $|\Delta_1| = 8.44$ meV, $|\Delta_2| = 15.26$ meV, $\Gamma_1 = 2.86$ meV, $\Gamma_2 = 2.79$ meV, $e = 0.13$. **d**, Two-band anisotropic Dynes model fitting. $|\Delta_1| = 9.66$ meV, $|\Delta_2| = 16.91$ meV, $\Gamma_1 = 1.54$ meV, $\Gamma_2 = 2.52$ meV, $e = 0.07$.

1.3. The Native Defects in 1-UC Fe(Se,Te)/STO

The main defect in 1-UC Fe(Se,Te)/STO is the dumbbell-like impurity, consisting of two adjacent top-layer Se/Te atoms (Fig. S4a). Since the height of the bright site is only 34 ± 5 pm (Fig. S4b), we interpret it as the Fe-centered vacancy in the underlying layer rather than extra Se/Te atoms, which is widely accepted in 1-UC FeSe^[5]. The spectra measured around the defect show that the coherence peak of the SC gap at negative bias side is remarkably enhanced, while the zero-bias conductance remains at zero (Fig. S4c). Commonly, when the defect-induced scattering potential is weak, the bound state lies close to the gap edge^[6]. Furthermore, the same type of defects in $(\text{Li}_{1-x}\text{Fe}_x)\text{OHFe}_{1-y}\text{Zn}_y\text{Se}$ is proved to be nonmagnetic because of the non-shift of the peak energy under the magnetic field of 11 T^[7]. Therefore, the dominant defects in 1-UC Fe(Se,Te) likely have weak and non-magnetic scattering potential, which is favorable to explicitly judging the gap-sign issue in 1-UC Fe(Se,Te) by the PR-QPI approach.

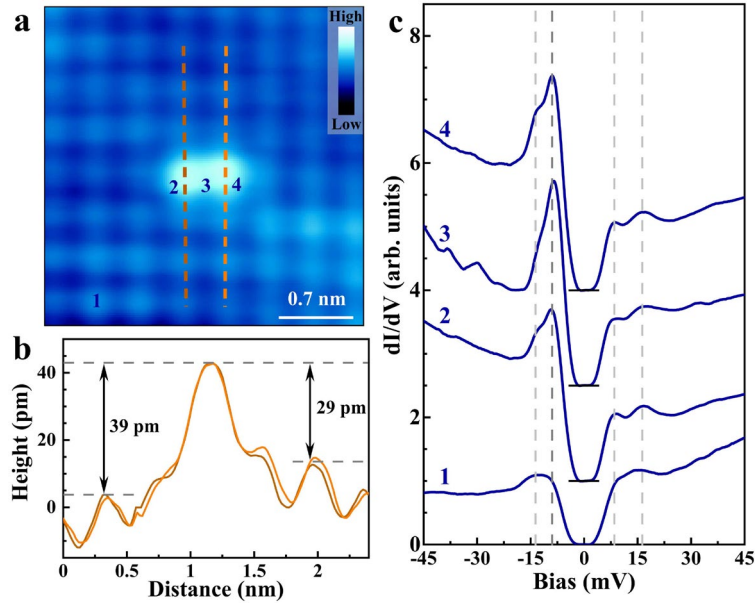


Figure S4. The native defects in 1-UC Fe(Se,Te)/STO. **a**, Topographic images of a dumbbell-like defect arising from Fe vacancy (3×3 nm², $V = 0.1$ V, $I = 0.5$ nA). **b**, Profile taken along the orange and brown curves in **a**, respectively, showing the height of the bright site is 34 ± 5 pm. **c**, Tunneling spectra ($V = 0.04$ V, $I = 2.5$ nA, vertically offset for clarity) obtained at the positions as numbered in **a**. The gray dashed lines indicate the two pairs of SC coherence peaks. The bound states are presented as the enhanced DOSs at the negative bias side near the gap edge.

2. Fourier Transform (FT-) Quasiparticle Interference (QPI) Data

2.1. Drift Correction by Lawler-Fujita Algorithm

We used Lawler-Fujita Algorithm to correct the distortion of $g(\mathbf{r}, E)$ ^[8], which is inferred from the simultaneously acquired topographic images. Due to the hysteresis and mechanical creep of piezoelectric actuator as well as the thermal drift, STM has an inevitable discrepancy between the STM

controller's model of the probe tip's location and the probe tip's true location over the surface^[9]. Fig. S5a and S5c typify a topographic image and the corresponding FT pattern, respectively. The inset in Fig. S5c shows the Bragg spot of the top Se lattice with noticeable noise. Furthermore, the upper and lower Bragg points obviously are not along the same vertical line, leading to non-orthogonality of the x/y axes. Figure S5b and S5d show the topographic image and the corresponding FT pattern after correction. Noise around the Bragg spot decreases dramatically and the line connecting upper and lower (left and right) Bragg points is strictly vertical (horizontal) passing through the center. The latter enables us to directly symmetrize the FT-QPI patterns (Fig. S6b).

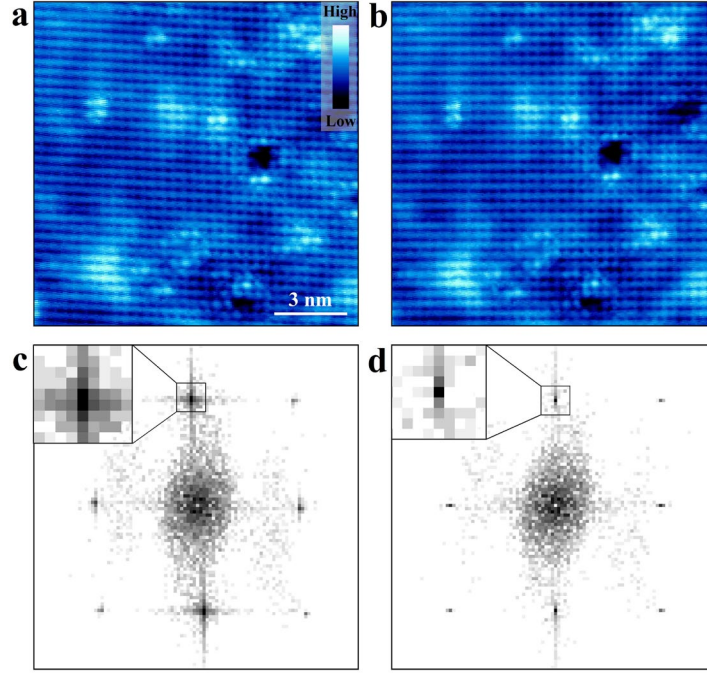


Figure S5. Topographic images and corresponding FT patterns. **a,b**, Topographic images before and after the correction ($13 \times 13 \text{ nm}^2$, $V = 0.04 \text{ V}$, $I = 2.5 \text{ nA}$), respectively. **c,d**, FT patterns of **a** and **b**, respectively. The insets are the zoom-in views of the Bragg spots.

2.2. FT-QPI Data Processing Steps

After correction of $g(\mathbf{r}, E)$, the obtained raw $|g(\mathbf{q}, E)| = |\text{FT-}g(\mathbf{r}, E)|$ (Fig. S6a) follows successive steps to optimize the signal-to-noise ratio. Firstly, we take advantage of the mirror symmetry axes of the Fermi surfaces (FSs) geometry in 1-UC Fe(Se,Te), which are horizontal and vertical in the 1-Fe BZ and diagonal in the 2-Fe BZ. Since we have already corrected the distortion of the non-orthogonality in the x/y axes (Fig. D5), we can directly symmetrize $|g(\mathbf{q}, E)|$ via diagonal axes. This step strikingly improves the visibility of the scattering rings (Fig. S6b). Secondly, we further implemented a four-fold rotational (C_4) symmetrization (Fig. S6c), which is commonly used for FT-QPI data processing in 1-UC FeSe^{[10],[11]}. Previous studies reported that the pronounced nematic order present in multilayer FeSe is suppressed in 1-UC FeSe and there is no indication for a C_4 symmetry breaking of the electronic structure^[12]. Even if the specific defects (Fig. S4) may have a C_2 scattering potential ($V_{xz,xz} \neq V_{yz,yz}$), which mainly tunes the intensity of the scattering rings without modifying the scattering wave vectors, it does not break the C_4 symmetry of the electronic structure in 1-UC Fe(Se,Te). Thus, we used the C_4 symmetrization. The last step is a Gaussian core subtraction of very

small scattering vectors around the center (Fig. S6d) as $|g_{new}(\mathbf{q}, E)| = |g_{raw}(\mathbf{q}, E)| [1 - A * \text{Gaussian}(\mathbf{q} = (0, 0), \sigma)]$, which restores the clarity of \mathbf{q}_1 scattering ring. The central peak around $\mathbf{q} = (0,0)$ chiefly develops from the randomly scattering defects and the long-range variations of the surface. Consequently, the Gaussian core subtraction corresponds to a long wavelength filter in real space, which does not affect the scattering signals of interest^{[13],[14]}. The parameters A and σ were adjusted slightly to make \mathbf{q}_1 scattering rings at different energies as clear as possible (Fig. S7).

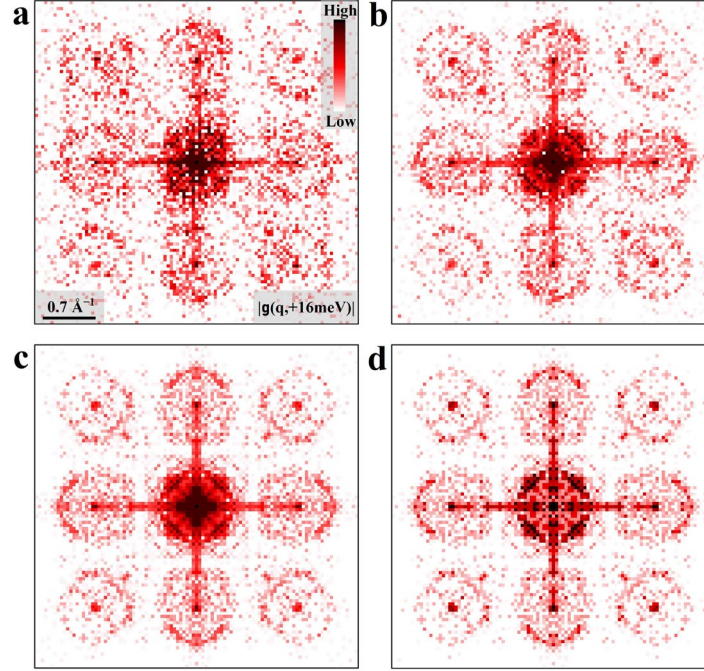


Figure S6. Exemplifying the FT-QPI pattern processing steps. **a**, Raw $|g(\mathbf{q}, E = 16 \text{ meV})|$ as obtained from distortion corrected $g(\mathbf{r}, E = 16 \text{ meV})$ shown in Fig. 2a. **b**, Mirror symmetrized $|g(\mathbf{q}, E = 16 \text{ meV})|$. **c**, Mirror symmetrized and C_4 symmetrized $|g(\mathbf{q}, E = 16 \text{ meV})|$. **d**, Mirror symmetrized, C_4 symmetrized, and Gaussian core subtracted $|g(\mathbf{q}, E = 16 \text{ meV})|$.

2.3. FT-QPI Data

Differential conductance mappings were measured individually for each pair of positive and negative energies ($\pm E$), and most scanning took about 1000 minutes. Limited by the duration time of scanning tunneling spectroscopy before next time liquid helium filling, $g(\mathbf{r}, E)$ at different E were inevitably taken at several different filed of views (FOVs). Thus, it is necessary to normalize the intensity $|g(\mathbf{q}, E)|$ at different E before plotting together (Fig. S11c). Besides, the variation of electronic structure between different areas in 1-UC Fe(Se,Te) film might induce the deviation of band dispersion at energy $E = 11 \text{ meV}$ and $E = 15 \text{ meV}$ (orange dashed curve in Fig. 3c).

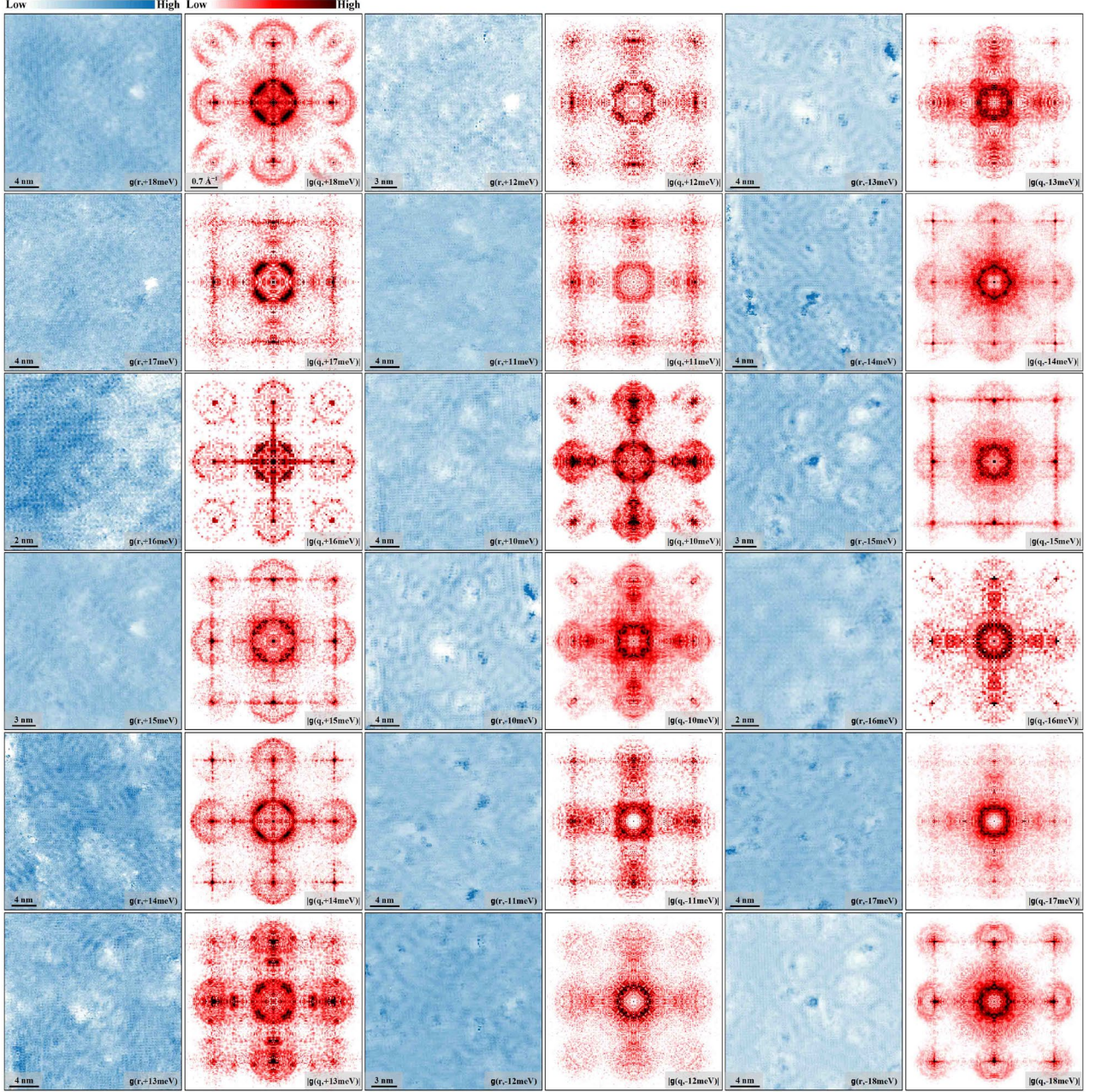


Figure S7. Differential conductance mappings $g(\mathbf{r}, E)$ and corresponding FT-QPI patterns $|g(\mathbf{q}, E)|$. Differential conductance mappings at different E were taken at different FOVs. $g(\mathbf{r}, E = \pm 16 \text{ meV})$ were taken in a $13 \times 13 \text{ nm}^2$ area. $g(\mathbf{r}, E = \pm 15 \text{ meV})$ were taken in a $22.3 \times 22.3 \text{ nm}^2$ area. $g(\mathbf{r}, E = \pm 14 \text{ meV})$ were taken in a $28.2 \times 28.2 \text{ nm}^2$ area. $g(\mathbf{r}, E = \pm 12 \text{ meV})$ were taken in a $20.7 \times 20.7 \text{ nm}^2$ area. Other $g(\mathbf{r}, E)$ were taken in $24 \times 24 \text{ nm}^2$ areas. Because the resolution of FT-QPI patterns $|\delta\mathbf{q}| = a_0/L \times (2\pi/a_0)$ is dependent on the length (L) of FOV, different $|g(\mathbf{q}, E)|$ has different \mathbf{q} -resolution. By selecting the proper number of pixels N , the side length of all $|g(\mathbf{q}, E)|$ is chosen to be $N|\delta\mathbf{q}| = 2.95 \times (2\pi/a_0)$.

3. The Relationship between Orbital Characters and Scattering Patterns

3.1. q_3 and q_2 Scattering Patterns

Here, we adopt the 1-Fe unit cell, which is more straightforward to analyze q_3 and q_2 scattering patterns. Accordingly, the x and y axes used for labeling d orbitals refer to the directions along nearest-neighbor Fe atoms. On the single elliptic electron pocket, the segments in the pole regions are

dominated by the d_{xy} orbitals, while the flat parts chiefly derive from the d_{xz}/d_{yz} orbitals (Fig. S8a)^[15]. The \mathbf{q}_3 and \mathbf{q}_2 patterns in our 1-UC Fe(Se,Te) (Fig. S8d) have exactly the same structures as that of previous works on 1-UC FeSe^{[10],[12]} and bulk (Li_{1-x}Fe_x)OHFeSe^{[7],[16],[17]}. This universality arises from the same geometry and orbital character of the FSs in the 1-UC FeSe-based system.

Specifically, \mathbf{q}_3 pattern, despite only differing from \mathbf{q}_1 pattern by a reciprocal vector in the 1-Fe BZ, shows an incomplete elliptic shape with long axis portion missing (Fig. S8d). Previous research has shown that \mathbf{q}_3 pattern at $(0, \pm 2\pi)$ and $(\pm 2\pi, 0)$ are mostly contributed by the intra-orbital scattering of d_{xz} orbital ($d_{xz} \leftrightarrow d_{xz}$) and d_{yz} orbital ($d_{yz} \leftrightarrow d_{yz}$), respectively^[12]. Whereas, \mathbf{q}_2 pattern, as far as we know, mainly consists of the intra-orbital scattering of d_{xy} orbital ($d_{xy} \leftrightarrow d_{xy}$). The structure of \mathbf{q}_2 pattern comprises four arcs^{[10],[17]}, but three of them usually connect jointly, only leaving the arc with smaller scattering vectors separately (Fig. S8d). There are three possible components in \mathbf{q}_2 pattern, including intra-orbital scattering of $d_{xy} \leftrightarrow d_{xy}$, intra-orbital scattering of $d_{xz} \leftrightarrow d_{xz}$ and $d_{yz} \leftrightarrow d_{yz}$, and inter-orbital scattering of $d_{xz} \leftrightarrow d_{yz}$, $d_{xy} \leftrightarrow d_{xz}$ and $d_{xy} \leftrightarrow d_{yz}$. The latter two components apparently have lower intensity compared to the first one. For one thing, $d_{xz} \leftrightarrow d_{xz}$ and $d_{yz} \leftrightarrow d_{yz}$ scatterings occur between the pole regions and the flat parts of the electron pockets. However, the composition of d_{xz}/d_{yz} orbitals is very limited at the pole regions of the electron pockets^[15], and accordingly the joint DOSs of this scattering are relatively small. Furthermore, the center of the arcs formed by $d_{xz} \leftrightarrow d_{xz}$ and $d_{yz} \leftrightarrow d_{yz}$ scattering should be along the directions at $\theta = 0^\circ + 90^\circ \times N$, $N = 0, 1, 2, 3$ (in 1-Fe BZ), which is contradictory to the arcs in \mathbf{q}_2 pattern centering along the directions at $\theta = 45^\circ + 90^\circ \times N$ (Fig. S8d). For the other, inter-orbital scatterings of $d_{xz} \leftrightarrow d_{yz}$, $d_{xy} \leftrightarrow d_{xz}$ and $d_{xy} \leftrightarrow d_{yz}$ are barely concerned in iron-based superconductors and have negligible effect on the QPI^{[14],[18],[19]}. Herein, we also do not consider inter-orbital scatterings. Then, only intra-orbital scattering of $d_{xy} \leftrightarrow d_{xy}$ in principle can significantly contribute to the intensity in \mathbf{q}_2 pattern. More importantly, considering the \mathbf{k} -space structure of d_{xy} orbital, $d_{xy} \leftrightarrow d_{xy}$ scattering do form the arc structure centering along the directions at $\theta = 45^\circ + 90^\circ \times N$. One may argue that the absence of $d_{xy} \leftrightarrow d_{xy}$ scattering in \mathbf{q}_3 pattern indicates the suppression of d_{xy} signals in STM measurements^{[12],[20]}. Note that \mathbf{q}_3 pattern at $(0, \pm 2\pi)$ is different from the \mathbf{q}_3 pattern at $(\pm 2\pi, 0)$ according to a finite Wannier function width^[12]. Thus, the particular Wannier function of d_{xy} orbital might selectively inhibit $d_{xy} \leftrightarrow d_{xy}$ scattering in \mathbf{q}_3 pattern.

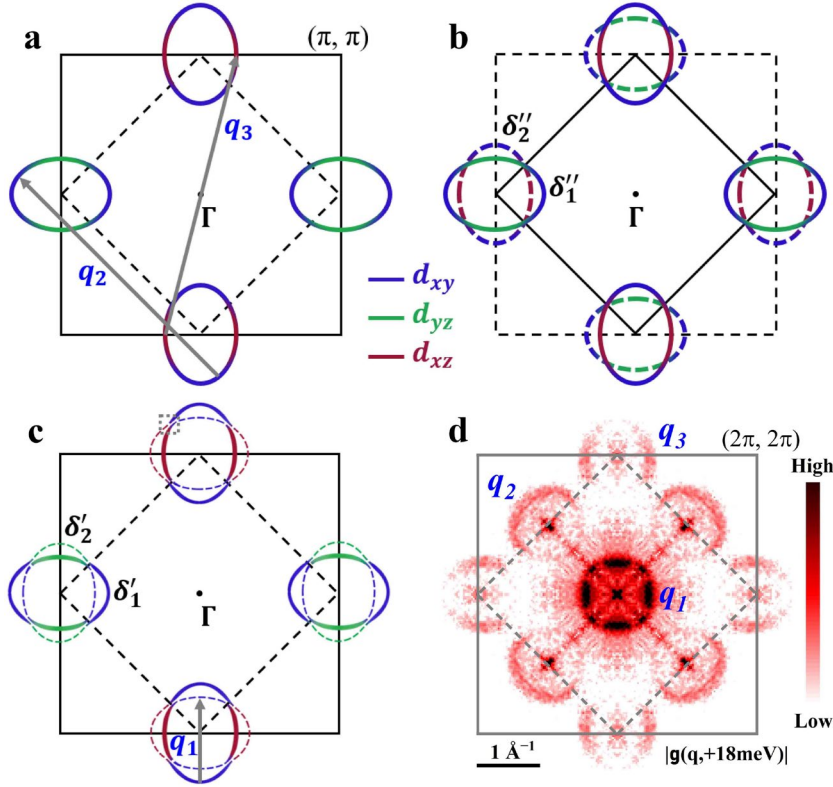


Figure S8. Orbital characters of electron pockets and relationship between Fe 3d orbitals and scattering patterns. **a**, FSs together with orbital characters in 1-Fe BZ (black solid lines). The gray solid arrows depict the representative scattering vectors corresponding to the scattering patterns in **d**. The orbital characters are shown in different colors. **b**, FSs in 2-Fe BZ (black solid lines). The dashed ellipses represent the folded band δ''_2 , which have the same line width as the original band δ'_1 (solid ellipses) to indicate the same spectral weight. **c**, FSs in unfolded BZ, obtained by unfolding the 2-Fe unit cell band structures, which is different from the original 1-Fe BZ since it incorporates the translational symmetry breaking potential arising from the staggered arrangement of Se/Te atoms^[22]. The dashed ellipses represent the unfolded (“shadow”) band δ'_2 , which have smaller line width than the original band δ'_1 (solid ellipses) to imply the weaker spectral weight. The small gray dashed square highlights the gap due to the band hybridization. The gray solid arrow depicts the inter-pocket scattering in q_1 pattern. **d**, FT-QPI pattern of $|g(q, E = 18 \text{ meV})|$, which rotates 45° compared to Fig. 4a, in order to correspond to the direction of 1-Fe BZ.

3.2. q_1 Scattering Pattern

While q_3 and q_2 scattering patterns can be well explained in 1-Fe BZ, the real symmetry of the 1-UC FeSe-based system actually dictates 2-Fe unit cell. It is widely accepted that, due to the breaking of translational symmetry, originating from the staggered arrangement of Se/Te atoms, bands in the 1st BZ of 1-Fe unit cell get ‘folded’ into the 1st BZ of 2-Fe unit cell (Fig. S8b). However, an underappreciated fact is that, regarding the weak symmetry breaking, experimental studies such as ARPES and STM normally show different band structures in *different* BZ of the 2-Fe unit cell rather than displaying all the bands in the 1st BZ of the 2-Fe unit cell^[21]. Therefore, for a direct comparison with experimental results, it is necessary to theoretically unfold the 2-Fe unit cell band structures. The unfolded band structures (Fig. S8c) are different from the nominal 1-Fe unit cell band structure (Fig. S8a), since it considers the translational symmetry breaking potential, which generates a “shadow” band δ'_2 in addition to the original band δ'_1 . More importantly, the “shadow” band δ'_2 in unfolded BZ is also different from the folded band δ''_2 in 2-Fe BZ (Fig. S8b)^[22]. For one thing, δ'_2 possesses

overall weak spectral weight, consistent with the experimental observation^[4], whereas the δ_2'' should have almost same spectral weight with the original band from the perspective of theoretical view. For another, the orbitals switch parity upon band unfolding, where the parity is defined as the mirror symmetry with respect to the Fe plane. For example, the odd parity orbitals of d_{xz} (red) and d_{yz} (green) in δ_2'' change to even parity orbital of d_{xy} (blue) in δ_2' , and vice versa. The orbital-parity switching is dictated by the glide-mirror symmetry, preserved by the staggered arrangement of Se/Te atoms^{[12],[22]}.

When investigating the \mathbf{q}_1 pattern, it is prerequisite to incorporate either the ‘‘shadow’’ band δ_2' (from experimental perspective) or the folded band δ_2'' (from theoretical perspective). Then, the band hybridization would open a gap at the intersection of the two elliptic-shaped electron pockets (highlight by the small gray dashed square in Fig. S8c). After that, the inner and outer electron pockets (δ_1 and δ_2 in Fig. 2b) are formed, where the pairing structure and the pairing symmetry such as ‘bonding-antibonding’ s_{\pm} -wave or ‘quasi-nodeless’ d-wave can be defined. It should be noted that the unfolded BZ has the superiority in demonstrating the inter-pocket scattering in \mathbf{q}_1 pattern (gray solid arrow in Fig. S8c), since it is intra-orbital scattering. In contrast, the inter-pocket scattering in \mathbf{q}_1 pattern is inter-orbital scattering $d_{xy} \leftrightarrow d_{xz}/d_{yz}$ in 2-Fe BZ (Fig. S8b), which should be suppressed^[18].

The last thing deserving clarification is that, despite the weak spectral weight of ‘‘shadow’’ band, the intensity of inter-pocket scattering is still noticeable and even dominate over the \mathbf{q}_1 pattern, which mainly benefits from the more coherent sign-changed scattering channel. In general, the intensity of FT-QPI pattern is determined by not only the DOSs, but also the Bogoliubov coherence factors, given by^[23]

$$v_i(\mathbf{k}) = \text{sign}[\Delta_i(\mathbf{k})] \sqrt{\frac{1}{2} \left[1 - \frac{\varepsilon_i(\mathbf{k})}{E_i(\mathbf{k})} \right]}, \quad u_i(\mathbf{k}) = \sqrt{\frac{1}{2} \left[1 + \frac{\varepsilon_i(\mathbf{k})}{E_i(\mathbf{k})} \right]} \quad (6)$$

where $E_k = \sqrt{\Delta_k^2 + \varepsilon_k^2}$ is the Bogoliubov spectrum of superconductors and i/j represents band. The scattering probability for a transition from the initial state (i, \mathbf{k}) to the final state (j, \mathbf{k}') is given by

$$W_{i \rightarrow j}(\mathbf{k}, \mathbf{k}') \propto |u_i(\mathbf{k})u_j^*(\mathbf{k}') \pm v_i(\mathbf{k})v_j^*(\mathbf{k}')|^2 \cdot |V(\mathbf{k}' - \mathbf{k})|^2 N_i(\mathbf{k})N_j(\mathbf{k}') \quad (7)$$

where V is scattering potential, N is DOSs, and the term $C(\mathbf{k}, \mathbf{k}') = |u_i(\mathbf{k})u_j^*(\mathbf{k}') \pm v_i(\mathbf{k})v_j^*(\mathbf{k}')|^2$ derives from the Fermi’s golden rule and chooses minus for scalar potential^{[23],[24]}. Since the scatters in our system are nonmagnetic (Supplementary Text 1.3), the value of $C(\mathbf{k}, \mathbf{k}')$ for the sign-changed scattering would be much larger than the one for the sign-preserved scatterings within the energy range of SC gaps ($\varepsilon_k \sim 0$). Correspondingly, the inter-pocket sign-changed scattering should have larger intensity than the intra-pocket sign-preserved scattering in \mathbf{q}_1 pattern, shown as the evident negative signals in PR-QPI patterns (Fig. 4 and Fig. S12).

4. Two Approaches to Extract Gap Structure

4.1. Determination of the Contour and Intensity of \mathbf{q}_1 Pattern

In order to more precisely locate the profile of \mathbf{q}_1 pattern (Fig. S9a) and extract the intensity correspondingly, we take several line cuts of $|g(\mathbf{q}, E)|$ along different radial direction (θ), with step size $\delta\theta = 3^\circ$ and azimuthal averaging over $\theta \pm 1^\circ$. Figure S9b shows typical line cuts of Gaussian-core subtracted FT-QPI intensity. The peaks with sizable broadening, can be well-fitted by Gaussian plus constant background. Sometimes, there are a few peaks closing to each other, like the line cut at $\theta = 6^\circ$. In this case, we choose the peak according to the empirical geometry of FSs^[15]. Figure S9c displays line cuts without Gaussian core subtraction, where there is an obvious slope. Correspondingly, we performed Gaussian fitting with linear background and obtained the almost same location of the

Gaussian peak. The variation between the two approaches is within $0.02 \pi/a_0$, smaller than the data resolution $|\delta\mathbf{q}| = 0.034 \pi/a_0$ in most FT-QPI patterns ($0.063 \pi/a_0$ in $|g(\mathbf{q}, E = 16 \text{ meV})|$). Therefore, the Gaussian core subtraction, despite slightly decreasing the absolute intensity of \mathbf{q}_1 pattern, does not modify the interested scattering wave vector. Herein, we used the Gaussian-core subtracted FT-QPI intensity to obtain Fig. 3c in order to better distinguish scattering vectors with short length (Supplementary Text 4.2), and used the raw FT-QPI intensity to obtain Fig. S11c, since it also focuses on the absolute intensity (Supplementary Text 4.3).

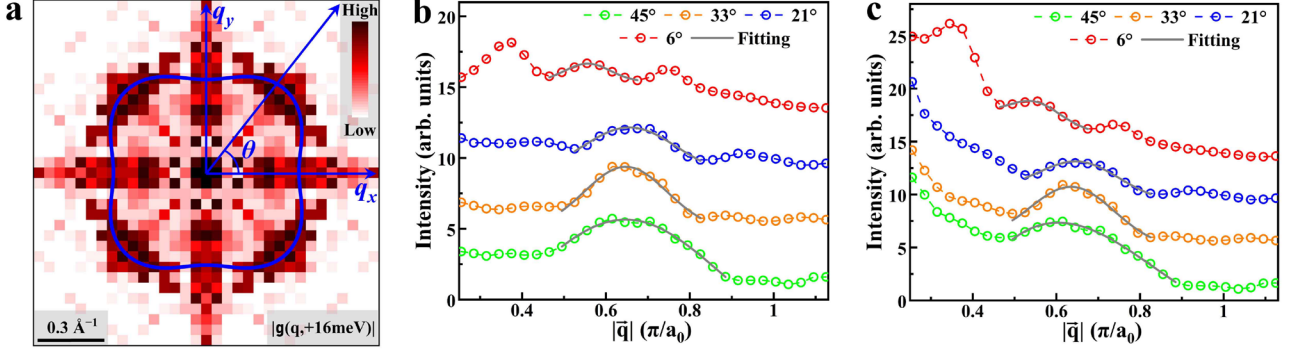


Figure S9. Extracting the \mathbf{q}_1 pattern. **a**, \mathbf{q}_1 pattern of $|g(\mathbf{q}, E = 16 \text{ meV})|$, where θ is defined relative to the q_x axis (corresponding to the $\Gamma\bar{X}$ direction in 2-Fe BZ). The blue closed curve fitted by $[R - r * \cos 4\theta]$ more accurately sketches the profile of \mathbf{q}_1 pattern. **b**, The line cuts of Gaussian-core subtracted FT-QPI intensity versus \mathbf{q} along different radial direction $\theta = 6^\circ, 21^\circ, 33^\circ$ and 45° (vertically offset for clarity). The gray solid lines are the Gaussian fits. The obtained positions of the Gaussian peak are $0.556 \pi/a_0$ (6°), $0.656 \pi/a_0$ (21°), $0.647 \pi/a_0$ (33°) and $0.647 \pi/a_0$ (45°). **c**, Same line cuts as **b** but for FT-QPI intensity without Gaussian core subtraction. The gray solid lines are the Gaussian fits plus linear background. The obtained intensities $I(\theta, E)$ are plotted in Fig. S11c after normalization. The obtained positions of the Gaussian peak are $0.552 \pi/a_0$ (6°), $0.667 \pi/a_0$ (21°), $0.652 \pi/a_0$ (33°) and $0.668 \pi/a_0$ (45°).

4.2. Determination of Gap structure and FS from Maximum-Intensity Points in the $|\mathbf{q}|$ -E plane

We used the Gaussian core subtracted FT-QPI patterns to obtain the intensity in Fig. 3c. The Gaussian core subtraction is unified as $|g_{new}(\mathbf{q}, E)| = |g_{raw}(\mathbf{q}, E)| [1 - 0.85 * \text{Gaussian}(\mathbf{q} = (0, 0), \sigma = 0.18 \pi/a_0)]$. Then we took line cuts along radial direction $\theta = 45^\circ$, averaged by the nearest-neighbor pixel, and normalized them individually by their averaged intensity within $[0.2, 0.8] \pi/a_0$.

Normally, the tips of the constant-energy-contours (CECs) lie on the same contour as the FS of the underlying normal state band structure, since the SC gap opens particle-hole symmetric relative to the FS^[14]. Then the determination of FS is purely a mathematical process. See Fig. S10 and Supplementary Equation (8,9).

$$x_1 = \frac{\sqrt{2}}{4} (|\mathbf{q}_M^{t_1}| + |\mathbf{q}_M^{t_2}|) \quad (8)$$

$$y_1 = \frac{\sqrt{2}}{4} (|\mathbf{q}_M^{t_1}| - |\mathbf{q}_M^{t_2}|) \quad (9)$$

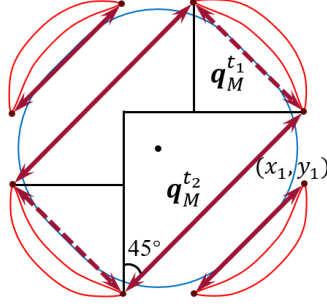


Figure S10. Sketch to obtain Fermi surface. Red contours show CECs of δ_2 . Red solid arrows depict the scatterings vectors associated with ‘banana’ tips along $\theta = 45^\circ$. Note that red dashed arrows have the same length as the shorter red solid arrows. The black lines are deliberately plotted to help understand the Supplementary Equation (8,9). The blue contour represents FS of δ_1 .

4.3. Determination of Gap structure and FS from the Iso-intensity Line in the θ -E plane

Another approach to distill gap structure also utilizes the scattering vectors associated with ‘banana’ tips. The difference lies in the selection of these vectors. While the approach in main body is based on the scattering along a specific high-symmetry direction (Fig. 3a), which only change length as energy varies, this approach focuses on scatterings at opposite side ($\mathbf{k} \leftrightarrow -\mathbf{k}$), which change direction as energy varies, shown as red arrows in Fig. S11a. Fig. S11b shows the schematic scattering intensity, deriving from the scattering between CECs at opposite side, where the maximum intensity points correspond to the scatterings between tips of CECs. Outside the CECs, ideally, there is no spectral weight, and the intensity shall reduce immediately and dramatically. Essentially, intensity $I(\theta, E)$ in Fig. S11b is a projection of the FT-QPI intensity $|g(\mathbf{q}, E)|$ onto the band dispersion $E(\mathbf{q}) = E(2\mathbf{k})$, and concurrently translates the coordinate from two-dimensional \mathbf{q} to one-dimensional θ . In this θ -E plane, the maximum-intensity points can be expressed as $\theta_M = 45^\circ \pm \theta_0 + 90^\circ \times N$ (Fig. S11b). As E increases from $|\Delta_2^{min}|$ to $|\Delta_2^{max}|$, θ_0 increases from 0° to 45° , and this curved trajectory contains the information about the gap structure.

In Supplementary Text 4.1, we extract the contour of \mathbf{q}_1 scattering pattern. Then, the normalized intensity on \mathbf{q}_1 scattering pattern at different E is shown in Fig. S11c (the data processing procedures can be found in the end of this section). Contrary to expectations, the maximum-intensity points are inconspicuous (or unreasonable) in Fig. S11c. We ascribe the absence of maximum-intensity points in experiments to the multiband effect. Recalling that the three sub-sets of \mathbf{q}_1 scattering pattern cannot be distinctively resolved in the QPI measurement, the \mathbf{q}_1 contour extracted above is more likely controlled by the inter-pocket scattering of $\delta_1 \leftrightarrow \delta_2$ rather than the desired intra-pocket scattering of $\delta_2 \leftrightarrow \delta_2$. This is also evidenced by the PR-QPI measurement (blue pixels in Fig. 4) and has substantial theoretical basis (see Supplementary Text 3.2 for the discussion on Bogoliubov coherence factors). In addition, intra-pocket scattering of $\delta_1 \leftrightarrow \delta_1$ also contributes to the intensity on \mathbf{q}_1 scattering pattern, especially around the $\Gamma\tilde{X}$ direction, where the three sub-sets merge. This further diminishes the distinction of the maximum-intensity points.

Although the maximum-intensity points are obscure and hard to precisely discern, there is still possible to roughly approximate the gap structure^[16]. Note that the black dashed curve in Fig. S11b depicts an iso-intensity line, which has a similar line shape as the curve connecting maximum intensity points. The intuition that FT-QPI intensity is suppressed along gap maximum direction (when $E < \Delta_{max}$), and the location where FT-QPI intensity first emerges would be associated with gap minimum

direction, is widely accepted^[14,41]. The iso-intensity line approximation is essentially a simplified way to make this intuition quantitative. Regarding the selection of the iso-intensity line, we chose the intensity I_0 to match the maximum of the anisotropic gap $|\Delta_2^{max}| = 18$ meV, which can be recognized from the average tunneling spectrum (Fig. S1c). Then the nominal iso-intensity line (white curve in Fig. S11c) was acquired via tracking the trajectory of energy thresholds (black hollow dots in Fig. S11c). The energy thresholds were extracted when the intensity, along E -axis direction at a fixed θ , starts to be larger than I_0 . One can see that the iso-intensity line clearly outlines the intensity profile associated with the evolution of the CECs and yields the gap minimum $|\Delta_2^{min}| = 11.6$ meV (Fig. S11c). We show the approximated gap structure and FS, obtained by iso-intensity line approach, in Fig. S11d. The anisotropic gap structure is consistent with the result in Fig. 3d, although the shapes of FS show some difference. The FS obtained by iso-intensity approach is almost circle-shape (Fig. S11d), which looks quite similar to the inter-pocket scattering pattern in theoretical simulations^{[7],[10]}. This once again indicates the intensity in Fig. S11c comes from the inter-pocket scattering. Note that the iso-intensity approach is merely an approximation of gap structure, since the FT-QPI intensity not only is related to the gap structure, but may also be influenced by the variations in the orbital character^{[15],[18]}.

Finally, we introduce the normalization process of $I(\theta, E)$, which is implemented in two steps. Firstly, we individually divided the raw intensity by its averaged intensity $I_{new}(\theta, E) = I_{raw}(\theta, E)/I_b(E)$. The averaged intensity is calculated within the concentric circles area $|\mathbf{q}_{min}^c(E)| < |\mathbf{q}(E)| < |\mathbf{q}_{max}^c(E)|$, where $|\mathbf{q}_{min}^c(E)|$ and $|\mathbf{q}_{max}^c(E)|$ are the minimum and maximum modulus of scattering vectors on the extracted contour $\mathbf{q}^c(\theta, E)$, respectively. This procedure aims to eliminate the influence of different scattering potential, deriving from the varying number and position of defects in QPI measurement at different FOVs. Using the \hat{T} -matrix approach^[6], the intensity of FT-QPI pattern is given by

$$g(\mathbf{q}, \omega) = -\frac{1}{\pi} \sum_{i,j} \text{Tr} \text{Im} \int \frac{d^2k}{(2\pi)^2} (\tau_0 + \tau_3) \hat{G}_i^0(\mathbf{k}, \omega) \hat{t}(\omega) \hat{G}_j^0(\mathbf{k} + \mathbf{q}, \omega) \quad (10)$$

where τ_0, τ_3 is the Pauli matrix, and $\hat{G}_{i/j}^0(\mathbf{k}, \omega)$ represents the Green's function for the band i/j . Here we use the general approximation that the $\hat{T}(\omega)$ matrix is momentum independent, which is a characteristic of point like s -wave scatterers, given by

$$\hat{T}(\omega) = \sum_j e^{iq \cdot \mathbf{R}_j} \left[1 - V_j \int \frac{d^2k}{(2\pi)^2} \hat{G}^0(\mathbf{k}, \omega) \right]^{-1} V_j \quad (11)$$

The summation is for all defects in the FOV. \mathbf{R}_j is the position of the defect j and V_j represents the matrix of its scattering potential. It is obvious that $\hat{T}(\omega)$ changes as the number and position of defects vary, consequently altering the intensity of the scattering pattern.

Secondly, though the procedure mentioned above can eliminate the variation of the $\hat{T}(\omega)$, it also wipes out the dependence of FT-QPI intensity on energy ω , originating from $\hat{G}^0(\mathbf{k}, \omega)$. Hence, we used the DOSs, characterized by the averaged tunneling spectrum in Fig. S1c, to restore the dependence on ω , via further multiplying the intensity by the square of the corresponding DOSs $I_n(\theta, E) = I_{new}(\theta, E) * [dI/dV(E)]^2$. The reason for this is that scattering intensity positively correlates with both the DOSs of initial state and final state.

After the normalization procedure, the intensity is virtually equivalent to

$$g'(\mathbf{q}, \omega) = \frac{\frac{1}{2} \text{Tr} \text{Im} \sum_{\mathbf{k}} (\tau_0 + \tau_3) \hat{G}^0(\mathbf{k}, \omega) \hat{T}(\omega) \hat{G}^0(\mathbf{k} + \mathbf{q}, \omega)}{\sum_{\mathbf{q}} \frac{1}{2} \text{Tr} \text{Im} \sum_{\mathbf{k}} (\tau_0 + \tau_3) \hat{G}^0(\mathbf{k}, \omega) \hat{T}(\omega) \hat{G}^0(\mathbf{k} + \mathbf{q}, \omega)}} \cdot \left(\frac{1}{2} \text{Tr} \text{Im} \sum_{\mathbf{k}} (\tau_0 + \tau_3) \hat{G}^0(\mathbf{k}, \omega) \right)^2 \quad (12)$$

Therefore, we unified the FT-QPI patterns measured at different FOVs and simultaneously, albeit not strictly, recovered their energy dependence, making the intensity ready for direct comparison.

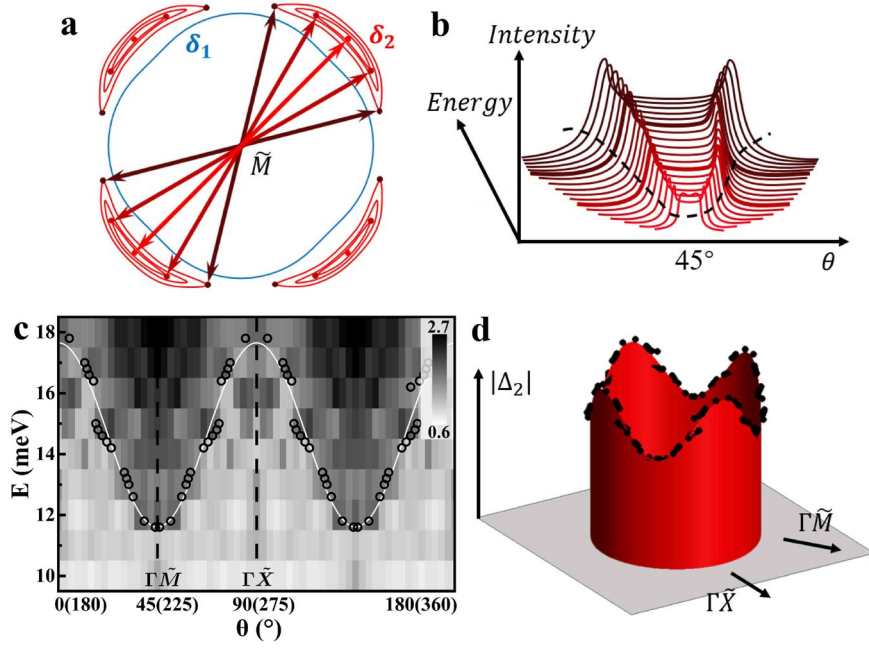


Figure S11. Determination of gap structure by iso-intensity line approach. **a**, The same schematic CECs as Fig. 3a. But in this case, the arrows associated with ‘banana’ tips change direction as the size of CECs enlarges. **b**, Schematic scattering intensity between CECs ($\delta_2 \leftrightarrow \delta_2$), where gradually darkened color indicates scattering intensity at increasing energy. The maxima correspond to the scatterings between the tips of CECs. The black dashed curve depicts the iso-intensity line, which has a similar line shape as the curve connecting maximum intensity points. **c**, Two-dimensional map of normalized $I_n(\theta, E)$. The black hollow dots locate the energy thresholds where the intensity along E -axis at a fixed θ start to be larger than $I_0 = 1.475$. The white curve, which is the nominal iso-intensity line, schematically depicts the trajectory of these energy thresholds. **d**, The approximation for gap structure (black solid dots) on the simultaneously obtained FS of δ_2 , following the iso-intensity approach in **c**.

5. The Phase-referenced (PR-) QPI Approach

5.1. PR-QPI Results and Gap Symmetry in 1-UC Fe(Se,Te)/STO

Here, we proposed a PR-QPI approach based on the energy range between the gap maximum $|\Delta_2^{max}|$ and the gap minimum $|\Delta_2^{min}|$ rather than the energy of in-gap bound states induced by defects (see Supplementary Text 5.2 for theoretical analysis). This approach essentially originates from the HAEM approach^[26], which relies on an integrated quantity associated with the real part of anti-symmetrized inter-pocket scattering vectors. It is expected that this quantity will be coherently enhanced at the energy between two gaps^[13]. However, HAEM strictly requires one single non-magnetic impurity sited at the exact center in the FOV, obviously unsuitable for the surface with considerable native defects. In order to obtain a high \mathbf{q} resolution, we measured the QPI in large FOVs, which inevitably contains multiple defects. Therefore, we adopted the data process in defect-induced bound state QPI (DBS-QPI) approach, which defines the signals at positive and negative energies as^[27]

$$g_{pr}(\mathbf{q}, +E) = |g(\mathbf{q}, +E)| \cos(\theta_{\mathbf{q},+E} - \theta_{\mathbf{q},-E}) \quad (13)$$

$$g_{pr}(\mathbf{q}, -E) = |g(\mathbf{q}, -E)| \quad (14)$$

This data process can effectively eliminate the irrelevant phase coming from the position and the shape of the defects, and consequently still works for system with numerous defects. In this case, the

measured differential conductance mapping $g(\mathbf{r}, \pm E)$ can be viewed as the superposition of the standing waves from multiple scattering centers, given by

$$g(\mathbf{r}, \pm E) = \sum_j g^s(\mathbf{r} - \mathbf{R}_j, \pm E) \quad (15)$$

After the FT, the results are

$$g(\mathbf{q}, +E) = g^s(\mathbf{q}, +E) \sum_j e^{-i\mathbf{q}\cdot\mathbf{R}_j} \quad (16)$$

$$g_{pr}(\mathbf{q}, +E) = |g^s(\mathbf{q}, +E) \sum_j e^{-i\mathbf{q}\cdot\mathbf{R}_j}| \cos(\theta_{\mathbf{q},+E}^s - \theta_{\mathbf{q},-E}^s) \quad (17)$$

Therefore, this data process can offset the disturbing phase contribution stemming from the random distribution of defects and accurately reflect the phase information associated with SC gaps^[27]. However, this universality comes at a cost; it will bring a random amplitude factor ($|\sum_j e^{-i\mathbf{q}\cdot\mathbf{R}_j}|$) to PR-QPI signal, which recommends integrating $g_{pr}(\mathbf{q}, +E)$ over the inter-pocket scattering region to obtain the actual intensity^[28]. Nevertheless, we mainly concentrated on the phase information, i.e. the sign of the PR-QPI signals, regardless of the fluctuation of the signal amplitude. Moreover, recalling the anisotropic structure of the SC gap, the integral at the energy within $|\Delta_2^{min}|$ and $|\Delta_2^{max}|$ fails in principle. Hence, we analyzed our PR-QPI data without defining an integral quantity.

Figure S12 shows the PR- \mathbf{q}_1 patterns. At $E = 10$ meV, the PR- \mathbf{q}_1 pattern conspicuously presents positive signals, which is in accordance with the obtained gap minimum $|\Delta_2^{min}| \approx 10$ meV. As energy increases, the negative signals emerge in $\Gamma\tilde{M}$ directions and gradually expand to $\Gamma\tilde{X}$ directions along the contour of \mathbf{q}_1 pattern, indicating the anisotropic gap structure and the sign reversal gap symmetry in 1-UC Fe(Se,Te).

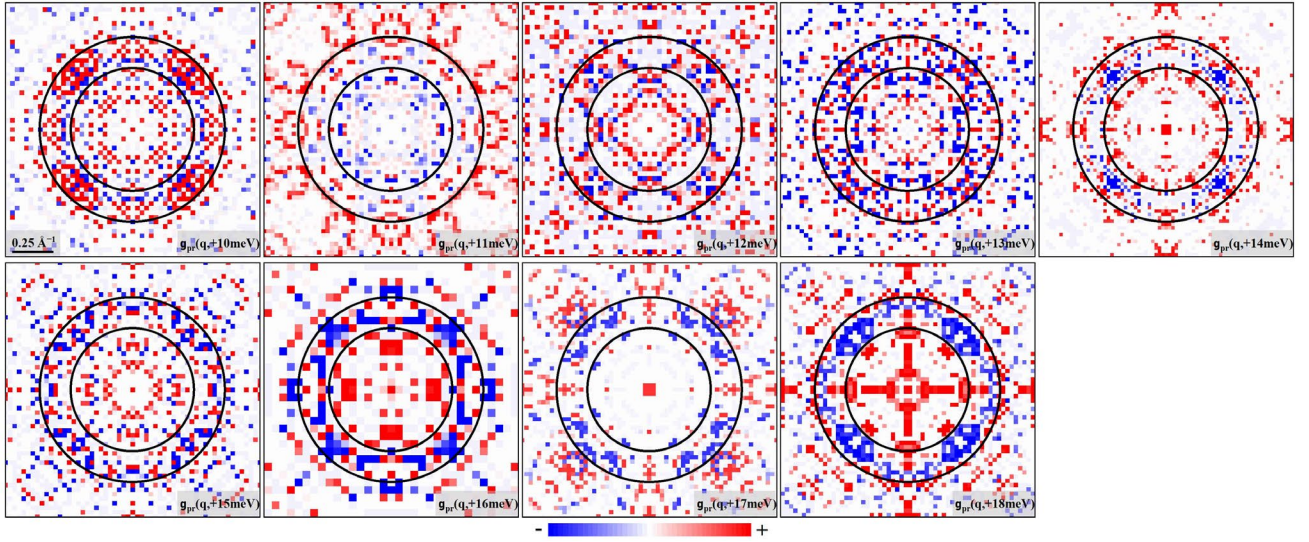


Figure S12. The central PR-QPI patterns $g_{pr}(\mathbf{q}, +E)$. The region within the concentric black circles schematically covers the \mathbf{q}_1 pattern, with inner radius as $0.5 \pi/a_0$ and outer radius as $0.75 \pi/a_0$. The resolution of each $g_{pr}(\mathbf{q}, +E)$ is same as the resolution of its $|g(\mathbf{q}, E)|$ (Fig. S7), and we chose the side length of all $g_{pr}(\mathbf{q}, +E)$ to be $2 \pi/a_0$.

Figure S13 shows schematics of two possible sign reversal gap symmetries and their simulated PR- \mathbf{q}_1 patterns. Note that the scattering vector along $\Gamma\tilde{X}$ direction is from sign-preserved gaps for ‘bonding-antibonding’ s_{\pm} -wave scenario (Fig. S13a), while the scattering vector along $\Gamma\tilde{X}$ direction

is from sign-changed gaps for ‘quasi-nodeless’ d -wave scenario (Fig. S13b). The simulation results can be found in Fig. S13c and S13d. Therefore, the red pixels along $\Gamma\tilde{X}$ directions especially at 18 meV (Fig. 4e) support ‘bonding-antibonding’ s_{\pm} -wave scenario and oppose ‘quasi-nodeless’ d -wave scenario.

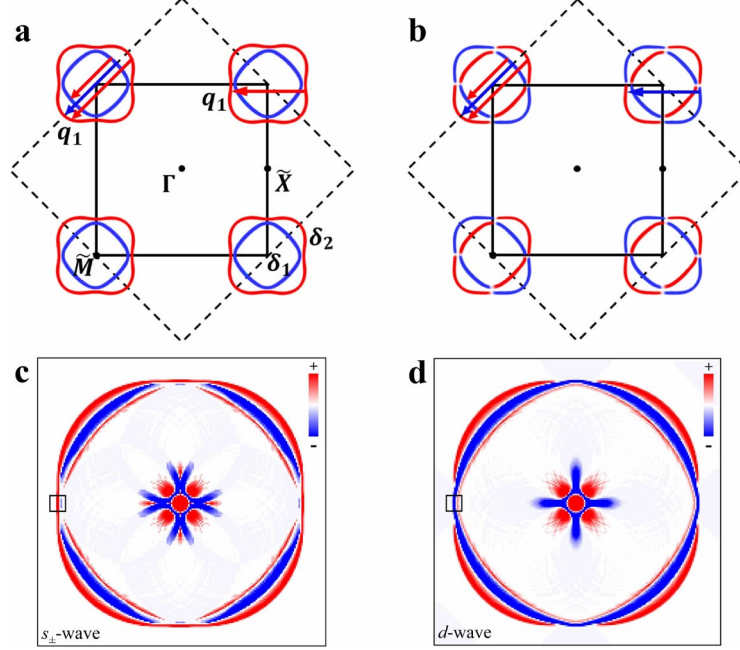


Figure S13. Schematics of possible sign reversal pairing symmetries in 2-Fe BZ and corresponding phase-referenced q_1 patterns. **a**, ‘Bonding-antibonding’ s_{\pm} -wave pairing state, where the gaps change sign between the inner pocket δ_1 (blue contour) and outer pocket δ_2 (red contour). The three sub-sets of q_1 pattern along the $\Gamma\tilde{M}$ direction consist of $\delta_1 \leftrightarrow \delta_1$ scattering, $\delta_1 \leftrightarrow \delta_2$ scattering, and $\delta_2 \leftrightarrow \delta_2$ scattering as shown by the three arrows, where two of them are sign-preserved (red arrows) and the other one is sign-changed (blue arrow). **b**, ‘Quasi-nodeless’ d -wave pairing state, where red and blue colors represent opposite signs of SC gaps. Note that there is no difference between ‘quasi-nodeless’ d -wave and ‘bonding-antibonding’ s_{\pm} -wave for scattering pattern along the $\Gamma\tilde{M}$ direction. However, the scattering pattern along the $\Gamma\tilde{X}$ direction mainly consists of sign-preserved scattering for ‘bonding-antibonding’ s_{\pm} -wave. Whereas, the scattering pattern along the $\Gamma\tilde{X}$ direction is dominated by sign-changed scattering for ‘quasi-nodeless’ d -wave. **c,d**, Simulated phase-referenced q_1 patterns according to the pairing symmetries in **a** and **b**, respectively. The black box marks the signal in the $\Gamma\tilde{X}$ direction, which shows red pixels (sign-preserved scattering) for ‘bonding-antibonding’ s_{\pm} -wave and blue pixels (sign-changed scattering) for ‘quasi-nodeless’ d -wave.

5.2. \hat{T} -matrix approach in Born approximation

We summarize the main results of our PR-QPI response within the \hat{T} -matrix approach in Born approximation^[6]. Out of convenience, we consider the case that one single non-magnetic defect sited at the center in the FOV, which can be extended to the multiple defects case as mentioned above. Theoretically, the zero-temperature intensity of the FT-QPI pattern is given by Supplementary Equation (10)^[18]. The Born approximation for the multiple scattering by a single impurity in the band and Nambu-Gorkov space is defined as

$$\begin{aligned}\hat{t}(\omega) &= V\tau_3 + V\tau_3 \int \frac{d^2k}{(2\pi)^2} \hat{G}^0(\mathbf{k}, \omega) V\tau_3 + \left[V\tau_3 \int \frac{d^2k}{(2\pi)^2} \hat{G}^0(\mathbf{k}, \omega) \right]^2 V\tau_3 + \dots \\ &= \left[I - V\tau_3 \int \frac{d^2k}{(2\pi)^2} \hat{G}^0(\mathbf{k}, \omega) \right]^{-1} V\tau_3 \approx V\tau_3\end{aligned}\quad (18)$$

where higher-order scatterings can be negligible, when the scattering potential is weak. The Nambu-Gorkov Green's function for band i is given by

$$\hat{G}_i^0(\mathbf{k}, \omega) = \frac{1}{\omega + i\eta - B_i(\mathbf{k})} \quad (19)$$

where η expresses the energy broadening and $B_i(\mathbf{k})$ is defined as

$$B_i(\mathbf{k}) = \begin{bmatrix} \varepsilon_i(\mathbf{k}) & \Delta_i(\mathbf{k}) \\ \Delta_i(\mathbf{k}) & -\varepsilon_i(\mathbf{k}) \end{bmatrix} \quad (20)$$

Regarding the ring-like structure of FT-QPI patterns, the intensities are contributed by the scatterings between \mathbf{k} and \mathbf{k}' located on the CECs, especially where the tangents of the CECs are parallel.

$$\mathbf{q} = \mathbf{k}' - \mathbf{k}, \quad \varepsilon_i(\mathbf{k}) = \sqrt{\omega^2 - \Delta_i^2(\mathbf{k})}, \quad \varepsilon_j(\mathbf{k}') = \sqrt{\omega^2 - \Delta_j^2(\mathbf{k}')} \quad (21)$$

Therefore, we only consider the parallel-tangent scattering hereinafter, which as far as we know dominates the scattering intensity. Since the intensity of a specific scattering vector \mathbf{q} now solely corresponds to the scattering between two local momenta, the Supplementary Equation (10) is greatly simplified as

$$g(\mathbf{q}, \omega) = -\frac{1}{\pi} \sum_{i,j} \text{Tr} \text{Im}(\tau_0 + \tau_3) \hat{G}_i^0(\mathbf{k}, \omega) \hat{t}(\omega) \hat{G}_j^0(\mathbf{k}', \omega) \quad (22)$$

Moreover, this simplification also refines the effect of the anisotropic SC gap, since the FT-QPI signal of a specific scattering vector \mathbf{q} now only relates to the fixed values of $\Delta_i(\mathbf{k}) = \Delta_i$ and $\Delta_j(\mathbf{k}') = \Delta_j$. Then the Supplementary Equation (22) can be calculated as

$$\begin{aligned}g(\mathbf{q}, \omega) &\approx -0.02V(\hbar v)^{-\frac{3}{2}} \kappa^{\frac{1}{2}} (\omega^2 - \Delta_i^2)^{-\frac{3}{8}} (\omega^2 - \Delta_j^2)^{-\frac{3}{8}} |\omega|^{-\frac{1}{2}} \eta^{-\frac{1}{2}} \\ &\cdot \left[\left(\omega + \sqrt{\omega^2 - \Delta_i^2} \right) \left(\omega + \sqrt{\omega^2 - \Delta_j^2} \right) - \Delta_i \Delta_j \right] \text{sgn}(\omega)\end{aligned}\quad (23)$$

where $\hbar v = d\varepsilon/dk$ is band dispersion and $\kappa = (d^2k/d\theta^2)/(dk/d\theta)^2$ is the curvature of CECs on Fermi level, both averaged over i, j . Besides, it requires $|\omega| > \max[|\Delta_i(\mathbf{k})|, |\Delta_j(\mathbf{k}')|]$ to promise the non-zero DOSs on \mathbf{k} and \mathbf{k}' . The most important conclusion from Supplementary Equation (23) is

$$\Delta_i \Delta_j < 0 \Leftrightarrow g(\mathbf{q}, \omega) g(\mathbf{q}, -\omega) < 0 \quad (24)$$

This is exactly the principle of our PR-QPI approach. The opposite sign indicates a nearly π phase shift between FT-QPI signals on the positive and negative energy sides, which yields $g_{pr}(\mathbf{q}, +E) < 0$.

Accordingly, the results of intra-pocket sign-preserved scattering are given by

$$g(\mathbf{q}, \omega) \approx -0.04V(\hbar v)^{-\frac{3}{2}} \kappa^{\frac{1}{2}} (\omega^2 - \Delta^2)^{-\frac{1}{4}} |\omega|^{-\frac{1}{2}} \eta^{-\frac{1}{2}} (\omega + \sqrt{\omega^2 - \Delta^2}) \text{sgn}(\omega) \quad (25)$$

$$g(\mathbf{q}, \omega) g(\mathbf{q}, -\omega) > 0 \quad (26)$$

The intensity in Supplementary Equation (25) is smaller than the sign-changed scattering intensity in Supplementary Equation (23), consistent with the conclusion from the joint density of states model, that the value of $C(\mathbf{k}, \mathbf{k}')$ for the sign-changed scattering would be much larger than the one for the sign-preserved scatterings (Supplementary Text 3.2).

In comparison, for magnetic scattering potential, the intensity is given by

$$g(\mathbf{q}, \omega) \approx -0.02V(\hbar v)^{-\frac{3}{2}}\kappa^{\frac{1}{2}}(\omega^2 - \Delta_i^2)^{-\frac{3}{8}}(\omega^2 - \Delta_j^2)^{-\frac{3}{8}}|\omega|^{-\frac{1}{2}}\eta^{-\frac{1}{2}} \cdot \left[\left(\omega + \sqrt{\omega^2 - \Delta_i^2} \right) \left(\omega + \sqrt{\omega^2 - \Delta_j^2} \right) + \Delta_i \Delta_j \right] \text{sgn}(\omega) \quad (27)$$

The conclusion is exactly opposite to the non-magnetic case as

$$\Delta_i \Delta_j < 0 \Leftrightarrow g(\mathbf{q}, \omega)g(\mathbf{q}, -\omega) > 0 \quad (28)$$

Another aspect is that whether the aforementioned conclusion changes for strong scattering potential when higher order scatterings need to be considered (beyond Born approximation). If the product of scattering potential and momentum integrated Green function approaches unity, the \hat{T} -matrix achieves a resonance and becomes close to ‘singularity’ (see Supplementary Equation (18)). An effect of this ‘singularity’ in \hat{T} -matrix comes into play if the imaginary part of the momentum integrated Green function is small, i.e. the density of states is small. This only emerges below the energy of the SC gap minimum, where the density of states changes strongly. Therefore, the presence of ‘singularity’ could diminish the amplitude of the PR-QPI signals near $|\Delta_2^{min}|$, and yet leaves the PR-QPI signals at higher energies mostly unaffected. Moreover, in our model, the ‘singularity’ effect is not enough to change the sign of the PR-QPI signals at $|\Delta_2^{min}|$ as long as the scattering potential V is significantly smaller than the energy scale associated with the bandwidth of the normal state electronic structure.

SI References

- [1] F. Li *et al.*, Interface-enhanced high-temperature superconductivity in single-unit-cell FeTe_{1-x}Se_x films on SrTiO₃. *Phys. Rev. B* **91**, 220503 (2015).
- [2] R. C. Dynes, V. Narayanamurti, J. P. Garno, Direct measurement of quasiparticle-lifetime broadening in a strong-coupled superconductor. *Phys. Rev. Lett.* **41**, 1509-1512 (1978).
- [3] R. C. Dynes, J. P. Garno, G. B. Hertel, T. P. Orlando, Tunneling study of superconductivity near the metal-insulator transition. *Phys. Rev. Lett.* **53**, 2437-2440 (1984).
- [4] Y. Zhang *et al.*, Superconducting gap anisotropy in monolayer FeSe thin film. *Phys. Rev. Lett.* **117** 117001 (2016).
- [5] C. Liu *et al.*, Extensive impurity-scattering study on the pairing symmetry of monolayer FeSe films on SrTiO₃. *Phys. Rev. B* **97**, 024502 (2018).
- [6] A. V. Balatsky, I. Vekhter, J. X. Zhu, Impurity-induced states in conventional and unconventional superconductors. *Rev. Mod. Phys.* **78**, 373-433 (2006).
- [7] Z. Du *et al.*, Sign reversal of the order parameter in (Li_{1-x}Fe_x)OHFe_{1-y}Zn_ySe. *Nat. Phys.* **14**, 134-139 (2018).
- [8] M. J. Lawler *et al.*, Intra-unit-cell electronic nematicity of the high- T_c copper-oxide pseudogap states. *Nature* **466**, 347-351 (2010).
- [9] M. P. Yothers, A. E. Browder, L. A. Bumm, Real-space post-processing correction of thermal drift and piezoelectric actuator nonlinearities in scanning tunneling microscope images. *Rev. Sci. Instrum.* **88**, 013708 (2017).
- [10] Q. Fan *et al.*, Plain s -wave superconductivity in single-layer FeSe on SrTiO₃ probed by scanning tunnelling microscopy. *Nat. Phys.* **11**, 946-952 (2015).
- [11] D. Huang *et al.*, Revealing the empty-state electronic structure of single-unit-cell FeSe/SrTiO₃. *Phys. Rev. Lett.* **115**, 017002 (2015).
- [12] D. Huang *et al.*, Bounds on nanoscale nematicity in single-layer FeSe/SrTiO₃. *Phys. Rev. B* **93**, 125129

- (2016).
- [13] P. O. Sprau *et al.*, Discovery of orbital-selective Cooper pairing in FeSe. *Science* **357**, 75-80 (2017).
- [14] M. P. Allan *et al.*, Anisotropic energy gaps of iron-based superconductivity from intraband quasiparticle interference in LiFeAs. *Science* **336**, 563-567 (2012).
- [15] A. Kreisel *et al.*, Orbital selective pairing and gap structures of iron-based superconductors. *Phys. Rev. B* **95**, 174504 (2017).
- [16] Z. Du *et al.*, Scrutinizing the double superconducting gaps and strong coupling pairing in $(\text{Li}_{1-x}\text{Fe}_x)\text{OHFeSe}$. *Nat. Commun.* **7**, 10565 (2016).
- [17] Y. J. Yan *et al.*, Surface electronic structure and evidence of plain *s*-wave superconductivity in $(\text{Li}_{0.8}\text{Fe}_{0.2})\text{OHFeSe}$. *Phys. Rev. B* **94**, 134502 (2016).
- [18] Y. Y. Zhang *et al.*, Quasiparticle scattering interference in superconducting iron pnictides. *Phys. Rev. B* **80**, 094528 (2009).
- [19] M. N. Gastiasoro, P. J. Hirschfeld, B. M. Andersen, Impurity states and cooperative magnetic order in Fe-based superconductors. *Phys. Rev. B* **88**, 220509 (2013).
- [20] T. Zhang *et al.*, Observation of Distinct Spatial Distributions of the Zero and Nonzero Energy Vortex Modes in $(\text{Li}_{0.84}\text{Fe}_{0.16})\text{OHFeSe}$. *Phys. Rev. Lett.* **126**, 127001 (2021).
- [21] W. Ku, T. Berlijn, C. C. Lee, Unfolding first-principles band structures. *Phys. Rev. Lett.* **104**, 216401 (2010).
- [22] Lin, C. H. *et al.*, One-Fe versus two-Fe Brillouin zone of Fe-based superconductors: creation of the electron pockets by translational symmetry breaking. *Phys. Rev. Lett.* **107**, 257001 (2011).
- [23] J. E. Hoffman, Spectroscopic scanning tunneling microscopy insights into Fe-based superconductors. *Rep. Prog. Phys.* **74**, 124513 (2011).
- [24] M. Maltseva, P. Coleman, Model for nodal quasiparticle scattering in a disordered vortex lattice. *Phys. Rev. B* **80**, 144514 (2009).
- [25] M. P. Allan *et al.*, Identifying the ‘fingerprint’ of antiferromagnetic spin fluctuations in iron pnictide superconductors. *Nat. Phys.* **11**, 177-182 (2015).
- [26] P. J. Hirschfeld, D. Altenfeld, I. Eremin, I. I. Mazin, Robust determination of the superconducting gap sign structure via quasiparticle interference. *Phys. Rev. B* **92**, 184513 (2015).
- [27] S. Chi *et al.*, Extracting phase information about the superconducting order parameter from defect bound states. Preprint at <https://arxiv.org/abs/1710.09088> (2017).
- [28] S. Chi *et al.*, Determination of the superconducting order parameter from defect bound state quasiparticle interference. Preprint at <https://arxiv.org/abs/1710.09089> (2017).